UC Davis
UC Davis Previously Published Works

Title

Numerical Modeling of Liquefaction-Induced Downdrag: Validation against Centrifuge Model Tests

Permalink

Journal

ISSN

Authors

Sinha, Sumeet K
Ziotopoulou, Katerina
Kutter, Bruce L

Publication Date

2022-12-01

DOI

Peer reviewed

Numerical Modeling of Liquefaction-Induced Downdrag: Validation against Centrifuge Model Tests

Sumeet K. Sinha, A.M.ASCE[1]; Katerina Ziotopoulou, M.ASCE[2]; and Bruce L. Kutter, M.ASCE[3]

Abstract: Earthquake-induced soil liquefaction can cause soil settlement around piles, resulting in drag load and pile settlement after shaking stops. Estimating the axial load distribution and pile settlement is important for designing and evaluating the performance of axially loaded piles in liquefiable soils. Commonly used neutral plane solution methods model the liquefiable layer as an equivalent consolidating clay layer without considering the sequencing and pattern of excess pore pressure dissipation and soil settlement. Moreover, changes in the pile shaft and the tip resistance due to excess pore pressures are ignored. A TzQzLiq numerical model was developed using the existing TzLiq material and the new QzLiq material for modeling liquefaction-induced downdrag on piles. The model accounts for the change in the pile's shaft and tip capacity as free-field excess pore pressures develop or dissipate in soil. The developed numerical model was validated against data from a series of large centrifuge model tests, and the procedure for obtaining the necessary information and data from those is described. Additionally, a sensitivity study on TzLiq and QzLiq material properties was performed to study their effect on the developed drag load and pile settlement. Analysis results show that the proposed numerical model can reasonably predict the time histories of axial load distribution and settlement of axially loaded piles in liquefiable soils both during and postshaking. **DOI: [10.1061/(ASCE)GT.1943-5606.0002930](https://doi.org/10.1061/(ASCE)GT.1943-5606.0002930).** © 2022 American Society of Civil Engineers.

Author keywords: Numerical modeling; Liquefaction; Piles; Downdrag; OpenSees; Centrifuge test.

Introduction

During earthquake shaking, piles in liquefiable soils can undergo settlements from the generation of excess pore pressures in the soil. Postshaking, the reconsolidation-induced soil settlement from excess pore pressures dissipation develops drag load and causes additional pile settlement. Generally, the pile resists the superstructure load (Q_f) by mobilizing positive skin friction along its shaft and tip resistance [Fig. 1(a)]. Excess pore pressures developed in the vicinity of a pile during shaking can reduce its shaft and tip capacity and cause settlement. Postshaking, the dissipation of excess pore pressures causes the associated reconsolidation and settlement of the soil, which in turn exerts negative skin friction, contributing drag load (Q_d) to the pile [Fig. 1(b)]. Consequently, the load on the pile increases, the length of the pile providing resistance decreases, more load is transferred to the shaft and tip below the neutral plane, and the pile settles [Fig. 1(c)]. The depth at which zero skin friction acts is known as the neutral plane [Fig. 1(b)]. At the neutral plane, the skin friction changes its direction from negative to positive, and the pile experiences its maximum axial load (Q_{np}) [Fig. 1(c)].

Blast-induced liquefaction studies over the last decade (Rollins and Strand 2006; Strand 2008; Rollins and Hollenbaugh 2015; Nicks 2017; Elvis 2018) have increased our understanding of the development of negative skin friction on piles in liquefiable soils. Rollins (2017) and Sinha et al. (2019) described factors (such as distribution of excess pore pressures, hydraulic boundary conditions, soil settlement, and pile tip conditions) that can influence the development of drag load and settlement in piles. Fellenius and Siegel (2008) used the unified pile design method to describe the effect of liquefaction and reconsolidation settlement relative to the static neutral plane (i.e., the neutral plane before liquefaction) on the developed drag load and settlement of the pile. Recently, Sinha et al. (2022a, b; Ziotopoulou et al. 2022) performed a series of centrifuge model tests on end-bearing piles and described the evolution of their axial load distribution and settlement during and postshaking [Figs. 2(c–f)]. Results showed that the negative skin friction was fully mobilized in the liquefiable layers and became equal to the interface shear strength. The settlement of the piles occurred mostly during shaking and was smaller during reconsolidation. Data from these tests can inform the development of approaches for modeling liquefaction-induced downdrag and estimating the magnitude of drag load and pile settlement, thus facilitating the design and evaluation of pile performance in liquefiable soils.

Various methods have been developed to account for the development of drag loads and estimate pile settlement in liquefiable deposits. Out of all of them, the neutral plane solution method (Fellenius 1972) has been most widely used. Fellenius and Siegel (2008), Vijayaruban et al. (2015), Muhunthan et al. (2017), and Fellenius et al. (2020) used the unified pile design method (Fellenius 2004) with zero negative skin friction in the liquefied zone to model liquefaction-induced drag load. In this method, the mobilized negative skin friction in the nonliquefiable layer is taken as equal to the interface shear strength. Rollins and Strand (2006) recommend taking the negative skin friction in the liquefiable layer as 50% of the positive skin friction before shaking. AASHTO (2020) and Caltrans (2020) recommend taking

[1]Postdoctoral Scholar, Dept. of Civil and Environmental Engineering, Univ. of California Berkeley, 408 Davis Hall, Berkeley, CA 94720 (corresponding author). ORCID: https://orcid.org/0000-0002-2011-4887. Email: sksinha@berkeley.edu

[2]Associate Professor, Dept. of Civil and Environmental Engineering, Univ. of California Davis, One Shields Ave., Davis, CA 95616. ORCID: https://orcid.org/0000-0001-5494-497X. Email: kziotopoulou@ucdavis.edu

[3]Professor Emeritus, Dept. of Civil and Environmental Engineering, Univ. of California Davis, One Shields Ave., Davis, CA 95616. ORCID: https://orcid.org/0000-0002-0628-1275. Email: blkutter@ucdavis.edu

© ASCE 04022111-1 J. Geotech. Geoenviron. Eng.

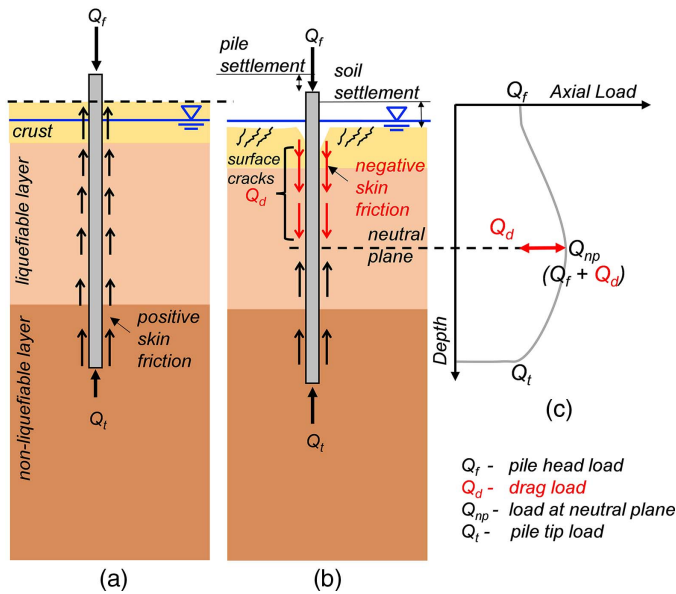J. Geotech. Geoenviron. Eng., 2022, 148(12): 04022111

Fig. 1. Illustration of liquefaction-induced downdrag on piles: (a) preearthquake shaking: distribution of pile shaft interface shear stresses and tip load; (b) during earthquake shaking: soil and pile settlement, shear stresses, neutral plane; and (c) after complete reconsolidation: pile axial load distribution.

the negative skin friction equal to the "residual soil strength" in the liquefiable layer. The Federal Highway Administration (FHWA; Hannigan et al. 2016) recommends using the neutral plane method with t–z and q–z springs calibrated from field tests. All the methods described previously model the liquefiable layer as a consolidating layer with a defined strength without considering the effects of

event sequencing and the pattern of excess pore pressure dissipation, soil settlement, and the evolution of soil shear strength during reconsolidation. Boulanger and Brandenberg (2004) modified the neutral plane method to account for the timing of the soil settlement and dissipation of excess pore pressures in liquefiable layers. The method accounted for the changes in shaft friction in the reconsolidating liquefied layer as a linear variation of excess pore pressures $(1 - r_u)$. Wang and Brandenberg (2013) used a TzLiq material to compute consolidation-induced drag load and downdrag settlement in clay, considering the change in excess pore pressures and effective stresses. The model assumed a constant mobilization of tip load equal to the undrained tip resistance. Wang et al. (2015) used Wang and Brandenberg's (2013) method to simulate postliquefaction reconsolidation downdrag of centrifuge test piles and obtained good agreements. The pile's tip resistance was assumed to be varying nonlinearly (based on pile settlement) between the undrained tip resistance existing before the earthquake and after the complete reconsolidation. A research front left open by the studies mentioned previously is the development of an effective stress-based pile tip resistance model where changes in the tip resistance are modeled as a consequence of excess pore pressure development or dissipation in the soil around the tip. The absence of such an effective stress-based pile tip resistance model has limited the complete simulation of the pile's response throughout a shaking event, that is, both during shaking and reconsolidation. As such, improvements are required to model the mechanism of liquefaction-induced downdrag, which can be further used to study and identify the controlling factors affecting the magnitude of drag load and pile settlement.

The goal of this paper is to develop and validate a numerical procedure to predict the behavior of piles where earthquake-induced downdrag is a consideration. It describes the development and validation of a TzQzLiq numerical model for capturing liquefaction-induced downdrag on piles. The TzQzLiq model uses zero-length elements and combines the existing TzLiq material with a new
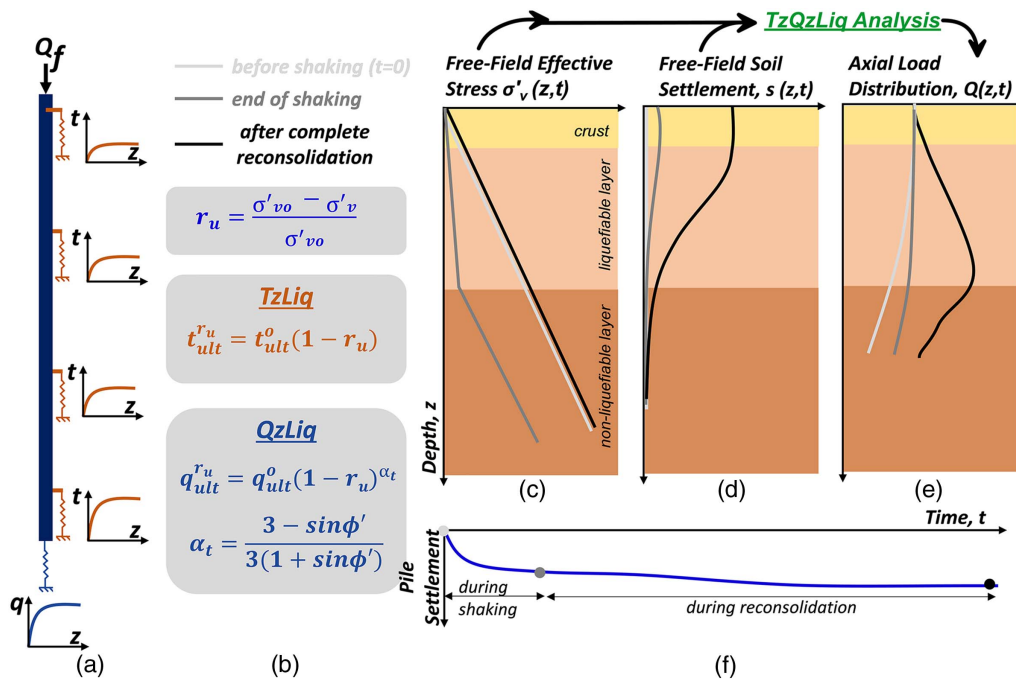

Fig. 2. Illustration of the TzQzLiq numerical model for modeling liquefaction-induced downdrag on piles using (a) the zero thickness interface elements with TzLiq and QzLiq materials. Model input parameters include properties of the pile; (b) TzLiq and QzLiq material properties; (c) isochrones of effective stress; and (d) soil settlement profiles. Model results include time histories of (e) axial load distribution; and (f) pile settlement.

QzLiq material to account for changes in the shaft and tip capacity of the pile and their stiffness as free-field excess pore pressures develop or dissipate in the soil. The TzQzLiq model is essentially a Winkler-type model, and the TzLiq and QzLiq materials are uncoupled. The paper first describes the selection of input parameters, the development of the QzLiq material, and the calibration process. Results from a series of centrifuge model tests on piles with different tip embedments and pile head loads are then introduced. The mechanism of liquefaction-induced downdrag on piles and the effect of an impermeable soil layer on the dissipation of excess pore pressure causing the impedance of drainage, equalization of excess pore pressures, and water film formation are illustrated. Procedures for obtaining the necessary information from the test data are described, which are later used to model the centrifuge test piles and validate the numerical model against the corresponding centrifuge data. Additionally, a sensitivity study of the properties of the TzLiq and QzLiq materials was performed to study their effect on the developed drag load and pile settlement.

Description of TzQzLiq Numerical Model

A TzQzLiq numerical model using TzLiq and new QzLiq materials [Fig. 2(a)] with zero-length elements was developed to model the response of piles in liquefiable soils. The model accounts for changes in the shaft (using a TzLiq material) and tip capacity (using a QzLiq material) of the pile as free-field excess pore pressures develop and dissipate in soil [Fig. 2(b)]. The overall numerical modeling process is illustrated in Fig. 2. A dynamic time history analysis was performed using the free-field effective stress $\sigma'_v(z, t)$ [Fig. 2(c)] and soil settlement, $s(z, t)$ [Fig. 2(d)] profiles to simulate the response of the pile. The results of the model include the time histories of axial load distribution [Fig. 2(e)] and settlement of the pile [Fig. 2(f)]. The model input parameters, which include pile cross-section, material and head loads (Q_f), TzLiq and QzLiq material properties, free-field effective stress and soil settlement profiles, and stages of modeling, are described in the following subsections.

Pile Properties and Loads

The required properties for modeling the pile include its cross-section and material properties and the superstructure dead load acting on its head. If the pile experiences cyclic axial loads during earthquake shaking, then those can be considered by applying a time history load on the pile. A separate analysis of the superstructure response under the design earthquake is required to estimate those cyclic axial loads. AASHTO (2020) suggests methods for determining seismic loads on bridges and their foundations. The present study used a linear elastic beam element to model the piles. If the axial loads exceed the elastic structural capacity of the pile, then nonlinear beam elements would be needed without affecting the remainder of the procedure herein.

TzLiq Material Properties

Boulanger et al. (1999) developed TzLiq material to model the reduction of the shaft capacity and shaft stiffness as a linear function of excess pore pressure ratio $(1 - r_u)$ [Eq. (1)]

$$t^{r_u}_{\text{ult}} = t^o_{\text{ult}}(1 - r_u) \tag{1}$$

where t^o_{ult} = ultimate shaft capacity when $r_u = 0$; and r_u = free-field excess pore pressure ratio around the shaft. The TzLiq material response is modeled as the constitutive response of t–z material

scaled in proportion to the excess pore pressure ratio $(1–r_u)$ (Boulanger et al. 1999). The initial elastic stiffness of the material is defined as $t^o_{\text{ult}}/2z_{50}$, where the constant z_{50} is the displacement required to mobilize 50% of the ultimate shaft capacity (t^o_{ult}). The constant z_{50} is kept independent of r_u, resulting in changes in the stiffness of the TzLiq material directly proportional to the change in its capacity ($t^{r_u}_{\text{ult}}$). Boulanger and Brandenberg (2004) used the TzLiq material to study the liquefaction-induced downdrag on piles in liquefiable soils.

The ultimate shaft capacity (t^o_{ult}) in soil layers can be obtained empirically using equations and correlations provided in AASHTO (2020) or can be calibrated from tests on interface shear strength and pile load tests. The z_{50} parameter essentially defines the stiffness of the shaft resistance. Fleming et al. (2008) showed that displacements of 0.5% to 2% of pile diameter are required to mobilize the shaft capacity. Sinha et al. (2022b) performed a series of centrifuge model tests and found that soil displacements of 1%–3% of the pile's diameter were sufficient to mobilize the total skin friction capacity. The nonlinear backbone curve for t–z material (Boulanger et al. 1999; Mosher 1984; Reese and O'Niel 1987) is a hyperbolic curve that takes displacement equal to about four times z_{50} to mobilize >90% of the ultimate capacity (t^o_{ult}). Thus, a z_{50} of 0.2%–0.5% of the pile's diameter can be assumed to model the stiffness of the TzLiq material.

QzLiq Material Properties

During shaking, loss of tip capacity and stiffness from excess pore pressures in the soil can cause settlements of piles. During reconsolidation, any settlement at the tip affects the development of drag load. Knappett and Madabhushi (2009) used load measurements from a series of centrifuge tests on piles in liquefiable soils and proposed an empirical model [Eq. (2)] to estimate the ultimate pile tip capacity in liquefying soil ($q^{r_u}_{t,\text{ult}}$) as a nonlinear function of the free-field excess pore pressure ratio (r_u) at a depth of the pile's tip

$$q^{r_u}_{t,\text{ult}} = q^o_{t,\text{ult}}(1 - r_u)^{\alpha_t}$$
$$\alpha_t = \frac{3 - \sin \phi'}{3(1 + \sin \phi')} \tag{2}$$

where $q^o_{t,\text{ult}}$ = ultimate tip capacity when $r_u = 0$; and the α_t = material constant, which, according to the empirical model of Knappett and Madabhushi (2009), only depends on the effective friction angle (ϕ') of the soil at the tip. Sinha (2022) performed several centrifuge tests on axially loaded piles in liquefiable soils and found a very good agreement with the previously proposed model [as defined in Eq. (2)]. Sinha (2022) observed that when the mobilized pile tip load reached the ultimate tip capacity ($q^{r_u}_{t,\text{ult}}$), the pile suffered significantly large settlements.

A new QzLiq material model following the evolution law of ultimate pile tip capacity ($q^{r_u}_{t,\text{ult}}$) with excess pore pressure ratio (r_u) [as shown in Eq. (2)] was developed in OpenSees (McKenna et al. 2010). The new QzLiq material model extends the existing QzSimple1 material model available in OpenSees. It models an ultimate load ($q^{r_u}_{t,\text{ult}}$) in compression and zero strength in tension. The QzSimple1 material models a nonlinear q–z pile's tip behavior with no effect of excess pore pressure ratio (r_u); that is, $\alpha_t = 0$ and $q^{r_u}_{t,\text{ult}} = q^o_{t,\text{ult}}$. The backbone curve of the QzSimple1 material model is described in Gajan et al. (2010). Like the TzLiq and PyLiq materials (as described in Khosravifar and Boulanger 2010), the new QzLiq material response is modeled as the constitutive response of a QzSimple1 with the capacity and stiffness scaled in proportion to the excess pore pressure ratio $(1 - r_u)^{\alpha_t}$.

The properties of the QzLiq material include the ultimate tip capacity ($q_{t,\text{ult}}^o$), the displacement (z_{50}) at which 50% of $q_{t,\text{ult}}^o$ is mobilized, the exponent (α_t) approximated from Eq. (2), and a time-series data of free-field effective stress (σ_v') at the pile's tip depth. The element internally evaluates the excess pore pressure ratio (r_u) from the provided mean effective stress data. The detailed documentation for QzLiq, TzLiq, and PyLiq material with implementation details and examples is available online (OpenSees Documentaion 2021). The TzLiq, PyLiq, and QzLiq material models implemented in OpenSees have been conventionally named TzLiq1, PyLiq1, and QzLiq1 materials, respectively. For simplicity (and given the lack of TzLiq2, PyLiq2, and QzLiq2 materials), they are called TzLiq and QzLiq materials.

The responses of the QzLiq material ($q/q_{t,\text{ult}}^o$) for displacement-controlled cyclic loading during shaking and monotonically increasing displacement during shaking and reconsolidation for different exponent values (α_t) are shown in Figs. 3(a and b), respectively. The figure also shows the input free-field excess pore pressure (r_u) and the normalized displacement (z/z_{50}) time-history at the pile's tip. Setting the exponent parameter as nil, that is, $\alpha_t = 0$, is equivalent to a q–z response where the mobilized tip resistance is unaffected by the excess pore pressure ratio (r_u). The larger the value of the exponent parameter (α_t), the greater the degradation of the tip resistance and its stiffness [as described in Eq. (2)] with excess pore pressure ratio (r_u). From the results of the cyclic loading case [Fig. 3(a)], it can be observed that the decrease in the mobilized tip resistance and stiffness is more significant for larger excess pore pressure ratio (r_u) and exponent values (α_t). The results of the monotonic loading case [Fig. 3(b)] during shaking show the competing effect of displacement (z/z_{50}) and excess pore pressure

ratio (r_u) on mobilized pile tip resistance ($q/q_{t,\text{ult}}^o$). At low r_u, the mobilized tip resistance can be seen to increase as displacement increases; however, as r_u becomes larger, the mobilized tip resistance starts to decrease. As a result, the two competing mechanisms ultimately mobilize a peak tip resistance, as shown in Fig. 3(b). As expected, the mobilized tip resistance is higher for smaller values of the exponent (α_t). In the reconsolidation phase, the dissipation of excess pore pressure and increase in tip displacement result in increased mobilization of tip resistance [Fig. 3(b)]. Similarly, the rate of mobilization of tip resistance is higher for smaller values of the exponent (α_t). In Fig. 3, the response of the tip with $\alpha_t = 0$ (shown in black) shows no effect of changes in excess pore pressure ratio (r_u).

Rather than reaching a limiting capacity, the pile tip resistance often continues increasing as penetration increases. Displacements of the order of 10% of the pile diameter are required to significantly mobilize the pile tip capacity (Fleming et al. 2008). In the absence of pile load test data, the tip capacity (estimated from empirical correlations with soil characterization data) is usually taken as the mobilized resistance for tip penetration equal to 10% of the pile diameter. Vijivergiya (1977) describes the nonlinear backbone curves for tip response in dense sand; where z_{50} is taken equal to 0.125 times the displacement required to mobilize the tip capacity. A pile load test could circumvent the need to assume values for the properties (q_{ult}^o, z_{50}) of the QzLiq material.

Free-Field Effective Stress and Soil Settlement Profiles

Time histories of free-field effective stress $\sigma_v'(z,t)$ and soil settlement $s(z,t)$ as a function of depth (z) are required to perform the
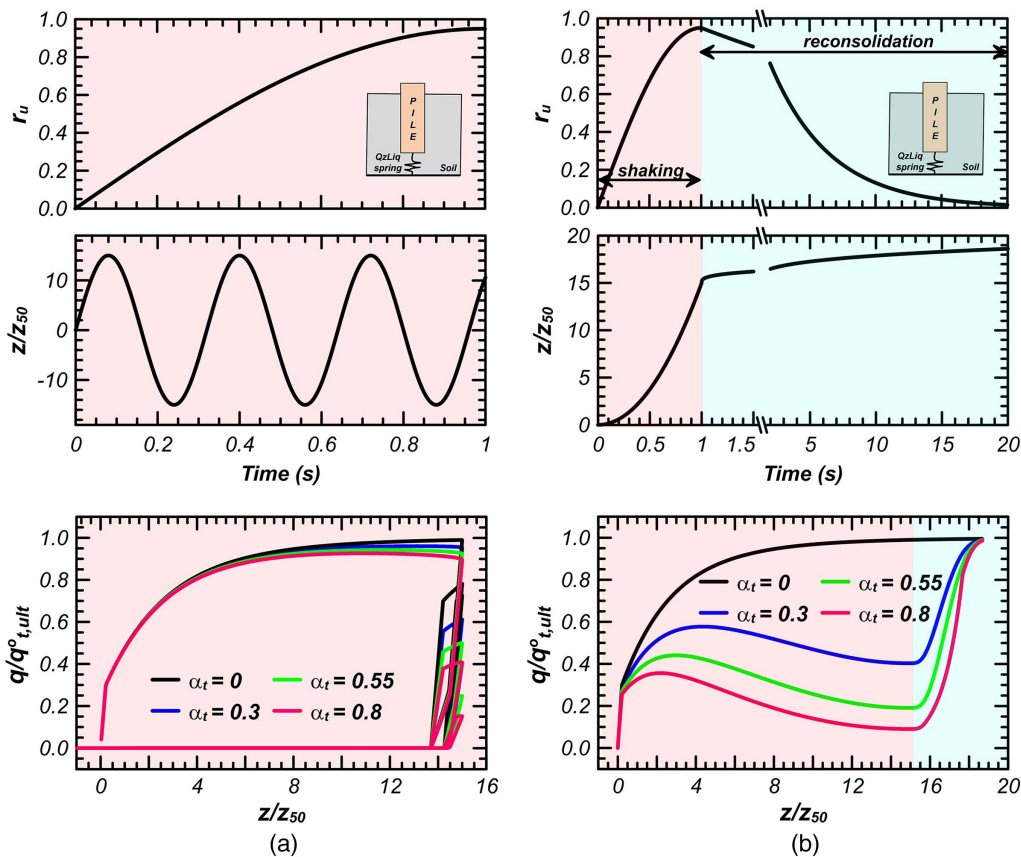

Fig. 3. Response of the QzLiq material ($q/q_{t,\text{ult}}^o$) for (a) displacement-controlled cyclic loading during shaking; and (b) monotonically increasing displacement during shaking and reconsolidation for different exponent values (α_t) of 0, 0.3, 0.55, and 0.8.

© ASCE 04022111-4 J. Geotech. Geoenviron. Eng.

J. Geotech. Geoenviron. Eng., 2022, 148(12): 04022111

proposed analysis of downdrag. For design purposes, these time histories may be obtained from a one-dimensional (1D) or two-dimensional (2D) site response analysis following a reconsolidation analysis with finite element or finite-difference software capable of capturing the salient features of the problem. For validation purposes, the time histories can also be determined from the measurements of a suitably instrumented field or model test.

Stages of Modeling

The simulation was performed in two analysis stages. In Stage 1, dead loads were applied, and the analysis yielded the initial (at $t = 0$) axial load distribution [Fig. 2(e)] for Stage 2. A dynamic time history analysis of the pile was performed in Stage 2 (Fig. 2), where the changes in the free-field effective stress $\sigma'_v(z, t)$ and soil settlement $s(z, t)$ profiles were dynamically applied to the TzLiq and QzLiq interface elements. In the case of seismic loads, a time history of axial load was applied to the pile's head.

Validation Using Centrifuge Model Tests

Centrifuge Model Test Data

Description of Centrifuge Model Tests
Two centrifuge model tests, SKS02 (Sinha et al. 2021a) and SKS03 (Sinha et al. 2021b), were performed on the 9-m-radius centrifuge at the Center for Geotechnical Modeling (CGM) at the University of California Davis. The tests were conducted at a centrifugal acceleration of 40 g. All units reported herein for the centrifuge test are in prototype scale following the centrifuge scaling laws by Garnier et al. (2007).

The SKS02 model consisted of two piles (0DPile and 5DPile) in a uniformly layered liquefiable deposit. The soil profile consisted of a 9-m-thick liquefiable loose sand layer ($D_R \approx 43\%$) sandwiched between a 4-m-thick layer of low permeable overconsolidated clay layer (with an undrained shear strength $s_u \approx 20$ kPa) on top and dense sand ($D_R \approx 85\%$) layer below [Fig. 4(a)]. The SKS03 model consisted of three piles (3DPileS, 3DPileM, and 3DPileL) in an interbedded soil deposit. The soil profile consisted of 1 m of Monterey sand, 2 m of clay crust ($s_u \approx 28$–35 kPa), 4.7 m of a loose liquefiable sand layer ($D_R \approx 40\%$), 1.3 m of a clayey silt layer (20% clay and 80% silt), 4 m of a medium dense sand layer ($D_R \approx 60\%$), and a dense sand layer ($D_R \approx 83\%$) [Fig. 4(b)]. The properties of all soil layers are summarized in Table 1. The models were instrumented with accelerometers, pore pressure transducers, and settlement sensors (linear potentiometers, as well as line lasers

and cameras for contactless location tracking) to monitor accelerations at various locations within the models, the generation or dissipation of excess pore pressures, and the settlements experienced by the piles and soil.

The models consisted of identical pipe piles with an outer diameter (D) of 635 mm and a thickness of 35 mm. The piles were instrumented with strain gauges in full-bridge configuration inside the pipe to measure the axial load distribution. The interface was made significantly rough to achieve full interface friction angle ($\delta = 30°$) (Sinha et al. 2022b). The 0D, 3D, and 5D naming annotations indicate the embedment depth of the pile tip; that is, the 0DPile had its tip placed at the bottom of the loose sand layer, whereas the 3D and 5D piles had their tips embedded 3 and 5 times their diameter into the dense sand. The static pile capacity for the 0DPile, 3DPiles, and 5DPile were estimated to be 2,700, 4,000, and 6,200 kN, respectively (Sinha et al. 2021a, b). The shaft capacity was calculated by integrating the interface shear strength along the length of the piles. The tip capacity was calculated as the median of the tip capacity estimated from the in-flight measured cone penetration resistance near the pile's tip using the empirical methods provided in AASHTO (2020), Lehane et al. (2005), Salgado and Lee (1998), and Titi and Abu-Farsakh (1999). A pile load test was also conducted on 3DPileS at 40 g on the centrifuge, which resulted in a static pile load capacity (estimated from De Beer's (1967) yield load method) of 3,800 and 4,500 kN, respectively, at the beginning and at the end of the centrifuge test. Both the 0Dpile and 5Dpile were loaded with a dead load of 500 kN [Fig. 4(a)], resulting in a static factor of safety of 5.4 and 12.4, respectively. The 3DPileS, 3DPileM, and 3DpileL were loaded with 500, 1,500, and 2,400 kN, resulting in a static factor of safety of 8, 2.7, and 1.7, respectively [Fig. 4(b)], with the annotations S, M, and L corresponding to the small, medium, and large dead head loads applied to produce the safety factors listed. The dead load on the piles was applied close to (about 1 m above) the ground's surface to limit the development of dynamic moments and lateral deflections during shaking.

The models were shaken with multiple earthquake motions with peak base accelerations (PBAs) ranging from 0.02 to 0.6 g. Results from two large shaking events, EQM_3 (third shaking event in SKS02) and EQM_4 (fourth shaking event in SKS03), are presented and later used to validate the developed numerical model. EQM_3 was a scaled Santa Cruz (Northridge 1994 earthquake) motion with a PGA of 0.24 g. EQM_4 was a long duration modified Santa Cruz motion (Malvick et al. 2002) consisting of one large pulse followed by five small pulses, scaled to produce a peak base acceleration of 0.45 g. The applied earthquake motions are shown in Fig. 4(c).

Table 1. Soil layer properties in two centrifuge model tests

Centrifuge Test	Soil layers	Relative density D_R[a] (%)	Thickness (m)	Saturated density (kg/m³)	Permeability k[b] (cm/s)
SKS02	Monterey sand	95	1	2,054	0.04
	Clay layer	—	4	1,713	0.000312
	Loose sand	42–44	9	1,968	0.026
	Dense sand	86–88	7.2	2,060	0.026
SKS03	Monterey sand	95	1	2,054	—
	Clay crust	—	2	1,700	0.000312
	Loose sand	40	4.7	1,971	0.026
	Clayey silt	—	1.3	2,000	0.00036
	Medium dense sand	55–60	4	2,019	0.022
	Dense sand	86–88	8	2,051	0.022

[a]Measured during model construction.
[b]Scaled to prototype scale and used in numerical analysis.

© ASCE 04022111-5 J. Geotech. Geoenviron. Eng.

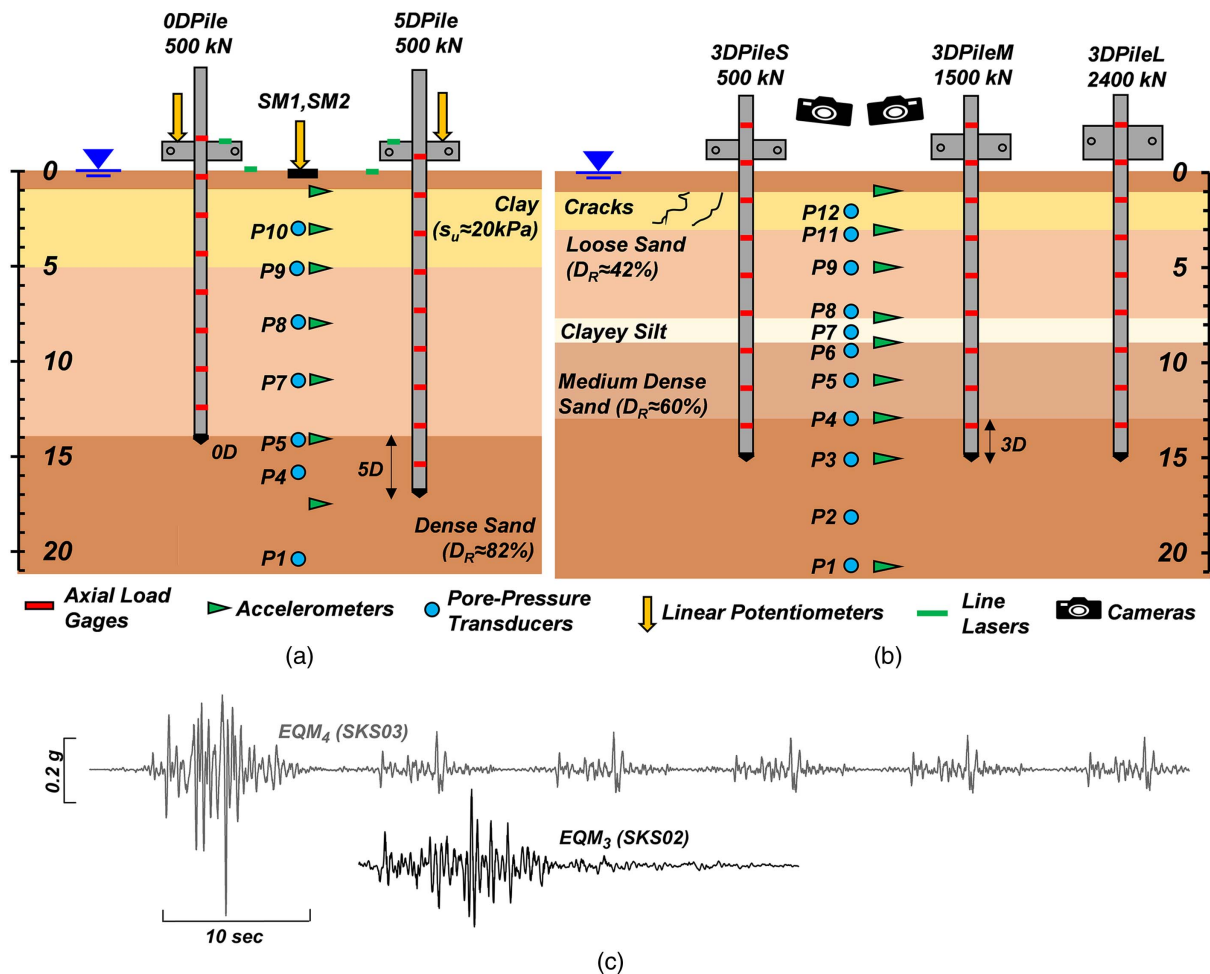J. Geotech. Geoenviron. Eng., 2022, 148(12): 04022111

Fig. 4. Cross-section view of the centrifuge model tests (a) SKS02; (b) SKS03; and (c) the applied earthquake motions EQM_3 and EQM_4.

Mechanism of Liquefaction-Induced Downdrag

The mechanism of liquefaction-induced downdrag is illustrated in Fig. 5 using the depth distributions of free-field effective stresses and axial load distribution in 5DPile as isochrones at various time instants during shaking event EQM_3 of centrifuge test SKS02. The initial (before shaking) and final (after complete reconsolidation) axial load distribution of all the piles are shown in Fig. 6. Time histories of excess pore pressures and soil and pile settlements for both models are shown in Fig. 7. During shaking, developed excess pore pressures decreased the drag load, shown as the isochrones of Fig. 5(b) shifting to the left. However, as excess pore pressures dissipated during the postshaking reconsolidation phase and soil settled, drag load was found to increase again, shown as the isochrones of Fig. 5(b) shifting to the right. The pile started with an initial drag load (at $t = 0$ sec) (and thus with an initial static neutral plane) developed from the previous shaking events [Figs. 5(b) and 6]. Generation of excess pore pressures (Figs. 5 and 7) during shaking decreased effective stresses [Fig. 5(a)] and resulted in the loss of the soil's shear strength. As a result, the drag load on the piles decreased, and consequently, the tip load also decreased [Fig. 5(b)]. However, the loss of free-field effective stress around the shaft and the tip below the neutral plane reduced the pile resistance and stiffness and caused settlement of the pile (Fig. 7). For 0DPile (in EQM_3 of SKS02) and 3DpileL (in EQM_4 of SKS03), the mobilized load at the tip reached closer to the reduced tip capacity causing excessive settlement of the piles (Fig. 7). When the soil fully
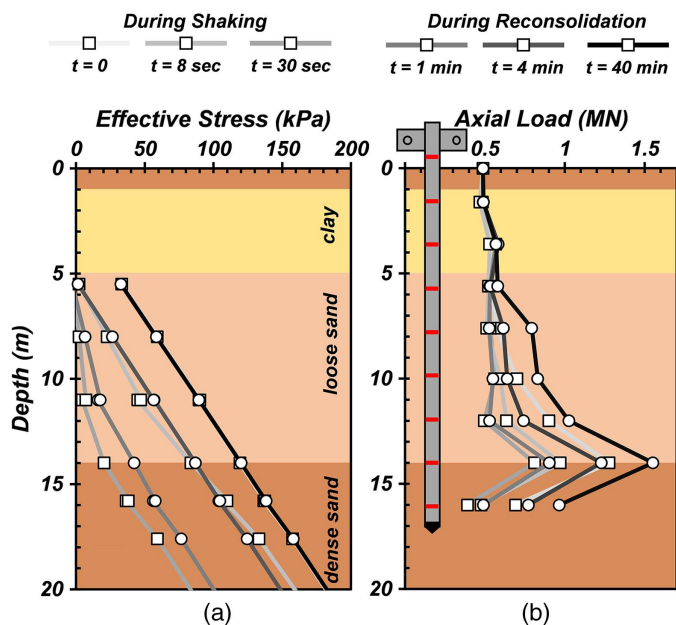

Fig. 5. Development of liquefaction-induced downdrag on 5DPile during shaking event EQM_3 of centrifuge test SKS02: (a) isochrones of free-field effective stress in soil; and (b) axial load distribution at selected times during and postshaking.
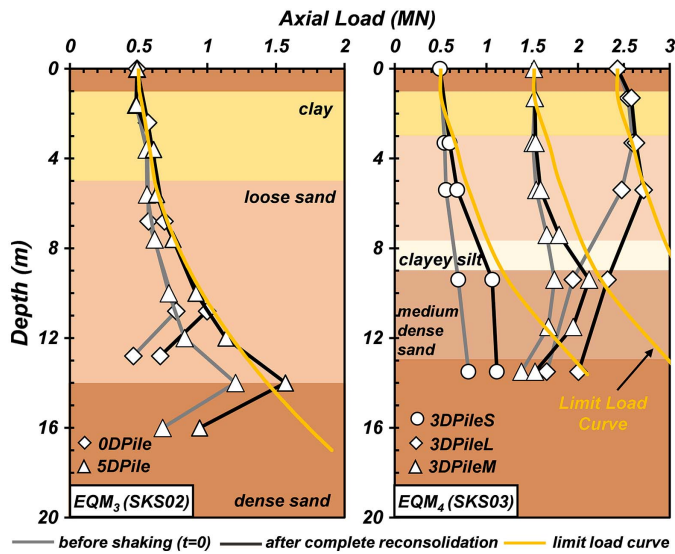
© ASCE   04022111-6   J. Geotech. Geoenviron. Eng.

J. Geotech. Geoenviron. Eng., 2022, 148(12): 04022111

Fig. 6. Axial load distribution in piles before and after shaking for shaking events EQM$_3$ (in centrifuge test SKS02) and EQM$_4$ (in centrifuge test SKS03) with their corresponding limit load curves.

liquefied [$\sigma'_v \approx 0$ at $t \approx 30$ s, (Fig. 7)], the drag load almost vanished (became zero), resulting in a constant vertical axial load distribution profile in the loose sand layer (5–12 m) [Fig. 5(b)]. Postshaking, as excess pore pressures dissipated and soil settled (Fig. 7), the drag load also increased [Fig. 5(b)]. Consequently, the load at the shaft and the tip below the neutral plane also increased [Fig. 5(b)]; however, the resulting pile settlement was smaller as the pile regained its tip capacity and stiffness. After

complete reconsolidation, the developed drag load was higher than its initial value before shaking (Figs. 5 and 6) because of the increased lateral stresses around the pile. The developed drag load was greater for the deeply embedded 5DPile and the lightly loaded 3DPileS. The final axial load distributions for the 0DPile and 5DPile (Sinha et al. 2021a) and 3DPiles (Sinha et al. 2021b) were found to be close to their corresponding limit load curves (Fig. 6), obtained from the sum of pile head load and the cumulative shaft capacity with depth. Most of the pile settlement occurred during shaking when the excess pore pressures in the soil were high. During reconsolidation, pile settlement was small (<10 mm) (Fig. 7).

Excess Pore Pressure Distribution and Soil Settlement

The clay and silt layers in the centrifuge tests contributed to interesting effects such as impedance of drainage and equalization of excess pore pressures. As shaking progressed, excess pore pressures rapidly increased and liquefied the loose sand layer (Fig. 7). When the shaking stopped, excess pore pressures quickly decreased (Fig. 7), equalized in the layers below the impermeable layers, and then slowly dissipated over time. It took more than 2 h for the complete dissipation of excess pore pressures in the sand and silt layers. In SKS02, the equalization of excess pore pressure occurred in the loose sand layer [Fig. 7(a)]. In SKS03, the equalization of excess pore pressures occurred in both the loose and medium dense sand layers. In SKS02, whereas the excess pore pressures dissipated in the loose sand between $t = 30$ s and $t \approx 2$ min, the surface did not settle [Fig. 7(a)]. It was only after $t \approx 2$ min that the surface started to settle [Fig. 7(a)]. Video recordings showed water coming to the surface from the sides of the container. The continuous dissipation of excess pore pressures with no surface settlement suggested the formation of a water film at the sand–clay interface (Sinha et al. 2022b). The continuous
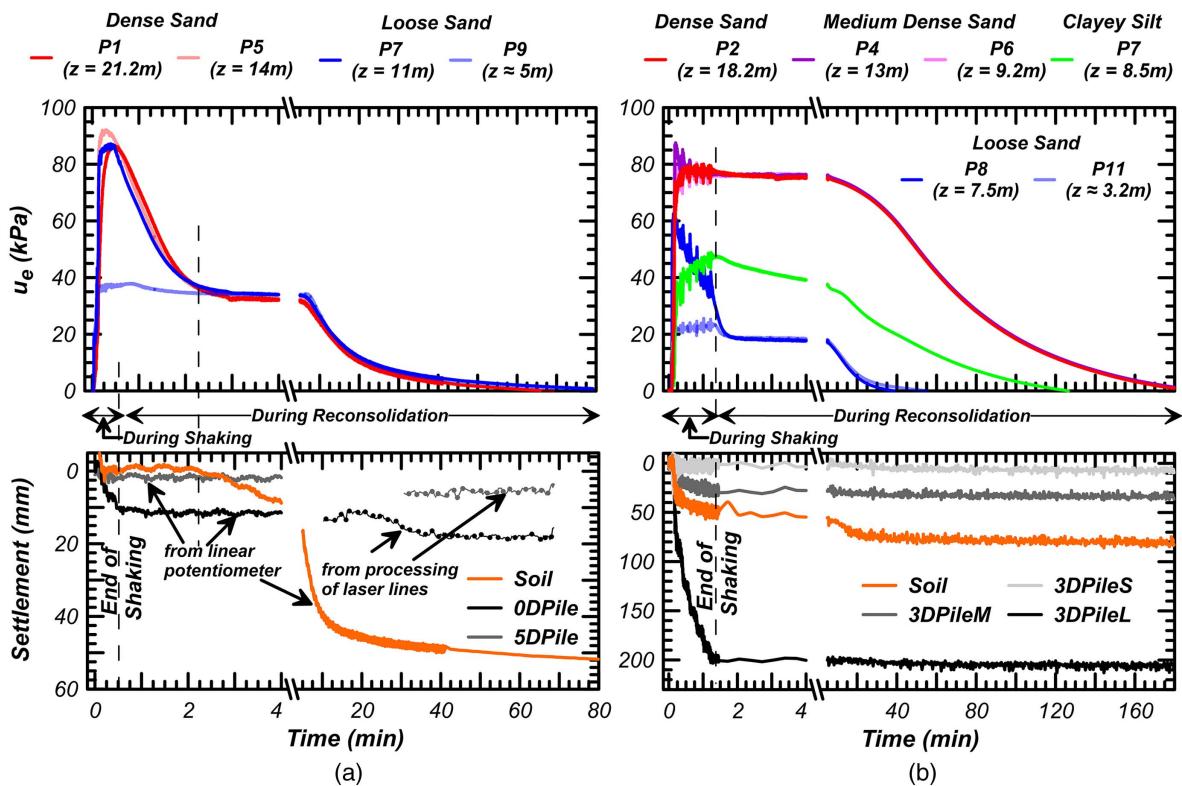

Fig. 7. Time histories of excess pore pressures as well as soil and pile settlement for shaking events: (a) EQM$_3$ (in centrifuge test SKS02); and (b) EQM$_4$ (in centrifuge test SKS03).

© ASCE 04022111-7 J. Geotech. Geoenviron. Eng.

J. Geotech. Geoenviron. Eng., 2022, 148(12): 04022111

dissipation of excess pore pressures with no surface settlement is consistent with the formation of a water filled gap at the sand–clay interface. The presence of the impermeable clay layer prevents drainage of water from the liquefied sand and water flowing up through the liquefied sand accumulates beneath the clay (Fiegel and Kutter 1994; Kokusho 1999, 2000; Malvick et al. 2008). In SKS03, no such sequences of surface settlements were observed. The soil surface kept continuously settling during the reconsolidation process. However, the relatively low permeability of the silt and clay slowed down the dissipation and resulted in equalized excess pore pressures in the loose and medium dense sand layers [Fig. 7(b)]. In order to investigate and study the development of water film formation (see the following section), a numerical model was developed and later used to understand the pattern of surface settlement in the SKS02 and SKS03 tests.

Although most of the soil settlement occurred during reconsolidation, soil layers suffered some immediate settlements during shaking. For the EQM_3 shaking in SKS02, the soil surface settled until $t = 30$ s [Fig. 7(b)]. For the EQM_4 shaking in SKS03, the immediate settlement occurred in the first 15 s of shaking [Fig. 7(b)]. The contours of surface settlement at the end of shaking (~70 s) and after complete reconsolidation (~3 h) of shaking event EQM_4 are shown in Fig. 8(a). The same figure also shows the time histories of soil settlement near the piles (3DPiles, 0DPile, and 5DPile) for the shaking events EQM_3 and EQM_4 [Figs. 8(b and c)]. Nonuniformities in the immediate settlements of soil layers resulted in uneven surface settlements [Fig. 8(a)]. The contours indicate larger settlements at the model's center compared to its boundaries. Investigations following the test suggested that in the curved g-field, the leveled surface of the Monterey sand layer and the layers beneath could be responsible for more immediate settlement at the center than at the boundaries [Fig. 8(a)]. The measured surface settlement was corrected by offsetting these immediate settlements during shaking ($t \approx 30$ s for both EQM_3 and $t \approx 15$ s for EQM_4) because it did not represent settlement from the dissipation of excess pore pressures. Corrected soil settlements were found similar across the model [Figs. 8(b and c)]. In the SKS03 model,

settlements measured at three distinct locations close to the individual piles matched well with each other [Fig. 8(b)]. In the SKS02 model, the corrected settlements at two distinct locations (SM_1 and SM_2) still had some differences [Fig. 8(c)]. It is possible that the presence of the water film at the sand–clay interface could have resulted in nonuniform settlements of the overlying soil (Fiegel and Kutter 1994). The mean of the corrected surface settlement is used for all further analyses.

Inverse Analysis of Measured Excess Pore Pressures to Obtain Soil Settlement Profiles

Inverse analysis of the recorded excess pore pressures was performed to obtain the time history of free-field soil settlement profiles, which were later used as an input in the numerical modeling of the centrifuge test piles for liquefaction-induced downdrag. In addition, a numerical model was developed to study the development of the water film at the sand–clay interface and its effect on surface settlements. Results from the analysis were later used to study the development of reconsolidation strains, surface settlement, and water film as excess pore pressures dissipated in the model (see discussion on the soil settlement in the "Results" section of the paper). This section describes the numerical modeling approach used for the inverse analysis and modeling of the water film at the sand–clay interface.

Following Malvick et al. (2008), inverse analyses of the measured excess pore pressures along the pore pressure transducer arrays (Figs. 4 and 7) were performed to estimate reconsolidation strains within the soil layers. The method used Darcy's law and 1D consolidation theory [Eq. (3)] to calculate the rate of reconsolidation strains ($\dot{\varepsilon}_v$)

$$i = \frac{\partial u_e(t)}{\gamma_w \partial z}$$

$$\dot{\varepsilon}_v = \frac{k}{\gamma_w} \frac{\partial^2 u_e(t)}{\partial z^2} \tag{3}$$
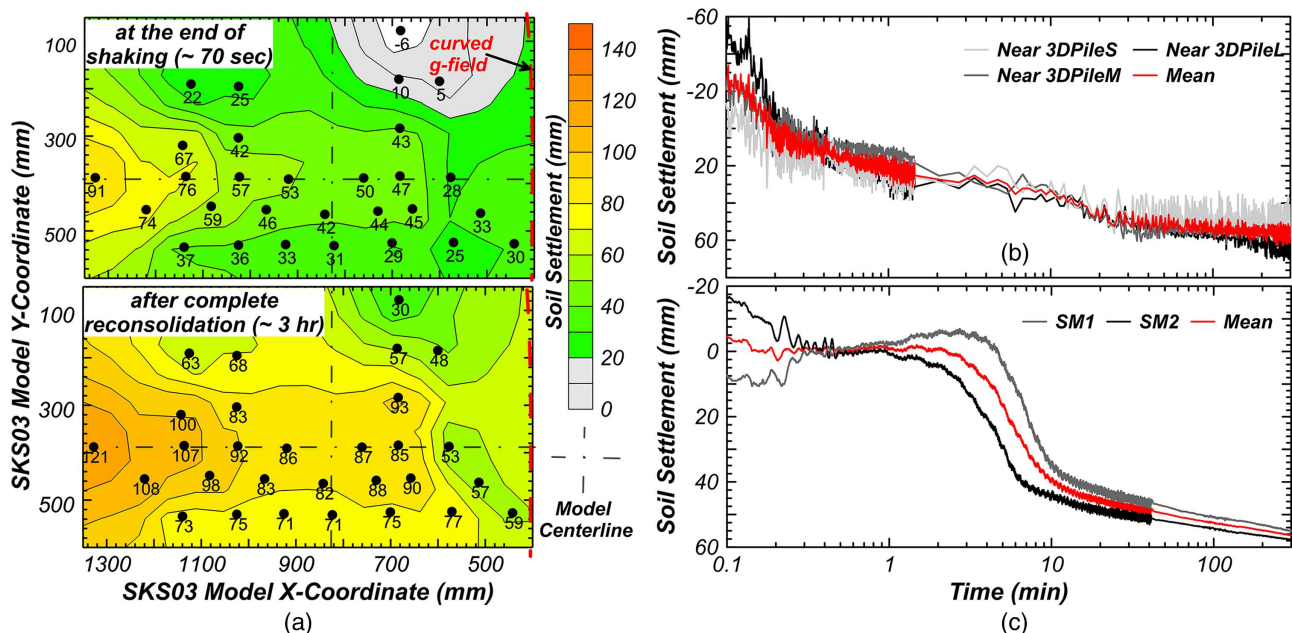

Fig. 8. (a) Contours of measured surface settlement for event EQM_4 of centrifuge test SKS03 towards the end of shaking (~70 s, top) and after complete reconsolidation (~3 h, bottom). Time history of soil surface settlements and their mean after correcting them for their immediate settlement at (b) $t \approx 15$ s for shaking event EQM_4; and (c) $t \approx 30$ s for shaking event EQM_3 (in centrifuge test SKS02).

where k = permeability of the soil; γ_w = unit weight of water; z = layer middepth; and $u_e(t)$ = excess pore pressure at time (t). A numerical smoothing function [Eq. (4)] was designed to numerically fit the measured excess pore pressures profiles

$$u_e(t) = \frac{a_0}{2a_1}\log(t^2 + 1) - \frac{a_0}{a_1}t \qquad \tan^{-1}t + a_3 z + a_4)$$

$$t = (a_2 - a_1 z) \tag{4}$$

where a_0, a_1, a_2, a_3, and a_4 = constants determined at each time (t) to numerically fit the experimental excess pore pressure profiles along with the boundary constraints. The impermeable boundary condition at the bottom of the container was enforced by making the hydraulic gradient zero ($i = 0$). Reconsolidation strain rates were integrated with time to obtain time histories of reconsolidation strains and soil settlements. The permeabilities of all the soil layers were assumed to be constant throughout the consolidation process. Their values are summarized in Table 1.

The formation of the water film layer at the sand–clay interface was calculated as the difference in the rate (q) of water entering ($q_{in} = k_{in}\, i_{in}$) and exiting ($q_{out} = k_{out}\, i_{out}$) the interface, where the permeabilities (k_{in} and k_{out}) and hydraulic gradients (i_{in} and i_{out}) are for the soil layers below and above the interface. A net inflow ($q_{in} - q_{out} > 0$) models the increase of water film thickness, whereas a net outflow ($q_{in} - q_{out} < 0$) models drainage of the water film. In the SKS02 test, the creation of favorable drainage paths from the sides of the model container (starting at $t \approx 2$ min) was modeled by increasing the permeability of the clay layer, which was found to have increased by a factor of 35 based on the calibration of the numerical results of surface settlement against measurements from the centrifuge test.

TzQzLiq Analysis of Centrifuge Model Test Piles

The TzQzLiq analysis of centrifuge model test piles was performed for the two large shaking events: EQM_3 in the SKS02 and EQM_4 in the SKS03 model. The ultimate capacity of the TzLiq material at different depths along the length of the pile was obtained from the limit load curves (Fig. 6). Backbone curves from Reese and O'Niel (1987) and Mosher (1984) were used to model the load transfer behavior of sections of piles in the sand and clay layers, respectively. The parameter z_{50} of the TzLiq material was taken as 0.3% of the pile diameter in the clay, silt, loose sand, and medium dense sand layers and 0.15% of the pile diameter in the dense sand layer (see also the section on TzLiq and QzLiq material properties). The q–z load transfer behavior was modeled with backbone curves from Vijivergiya (1977). Results from centrifuge pile load tests were used to calibrate the properties (q^o_{ult}, z_{50}) of the QzLiq material [shown in Fig. 11(a)]. The numerical and centrifuge test pile load test curves match quite well with the selected TzLiq and QzLiq material properties [Fig. 11(a)]. The constant (α_t) was taken as 0.55 calculated using Eq. (2) with an effective friction angle of $\phi' = 30°$. Table 2 summarizes the properties of the TzLiq and QzLiq material used in the numerical analysis. The time history of effective stress was obtained directly from the measurements of excess pore pressures in the centrifuge test (Fig. 7). The time history of soil settlement profiles was obtained from the results of the inverse analysis.

TzQzLiq analysis of the piles was performed in OpenSees (McKenna et al. 2010) with a mesh discretization of 0.1 m. The latest version of OpenSees (available from the GitHub repository at https://github.com/OpenSees/OpenSees) with the QzLiq material model implemented was used to perform the analysis. Stage 1 modeled the initial axial load distribution in the piles (Fig. 6) by

Table 2. TzLiq and QzLiq material properties used in the TzQzLiq analysis of piles

Soil Layers	z_{50} (%D[b])	Piles	z_{50} (%D[b])	$q^o_{t,ult}$ (kN)	α_t
	TzLiq[a] material properties		QzLiq material properties		
Clay and silt layers	0.30	0DPile	7	2,745	0.55
Loose, medium dense sand	0.30	5DPile	7	7,137	
Dense sand	0.15	3DPiles	9	4,576	

[a]t^o_{ult} at different depths along the length of the pile is obtained from the limit load curve shown in Fig. 5.
[b]Diameter of the pile.
Note: t^o_{ult} at different depths along the length of the pile is obtained from the limit load curve shown in Fig. 6. D = diameter of the pile.

applying the pile head load and iteratively finding the required soil settlement to develop the initial shear stresses. Stage 2 modeled liquefaction-induced downdrag on piles. Time histories of axial load distribution and pile settlement obtained from the analysis were compared to the results from the centrifuge tests to validate the numerical model. Additionally, a sensitivity study on the effect of the QzLiq constant (α_t) and stiffness of TzLiq materials in loose and dense sand ($z_{50,loose}$ and $z_{50,dense}$) was performed to evaluate their effect on the obtained drag load, neutral plane depth, pile settlement, and mobilized tip load. The study was performed by selecting the values of parameters (α_t, $z_{50,loose}$, and $z_{50,dense}$) one higher and one lower than that selected for numerical analysis ($\alpha_t = 0.55$, $z_{50,loose} = 0.3\%D$, and $z_{50,dense} = 0.15\%D$).

Comparison of Numerical Model Results with Centrifuge Test Data

Soil Settlement

Isochrones of excess pore pressure and reconsolidation strain rate profiles at selected times and the time histories of reconsolidation strain and soil settlement at selected depths for EQM_3 and EQM_4 are shown in Figs. 9 and 10, respectively. The plots show that the numerical smoothing function [Eq. (4)] used in the inverse analyses fitted the measured excess pore pressure profiles extremely well [Figs. 9(a) and 10(a)]. The figure also compares the predicted surface settlement with the centrifuge test results [Figs. 9(d) and 10(d)]. The surface settlement was obtained by subtracting the water film thickness from the total soil settlement. The predicted surface settlements from the inverse analyses matched quite well with the centrifuge test results [Figs. 9(d) and 10(d)]. The time histories of reconsolidation strains and soil settlement obtained from the inverse analyses helped understand the dissipation of excess pore pressures and observed surface settlement.

In the SKS02 centrifuge test, the analysis results showed water film formation at the sand–clay interface (Fig. 9). Results show that even though the impermeable clay layer hindered drainage, dissipation of excess pore pressures within the loose sand layer developed reconsolidation strains. The reconsolidation strains in the loose sand can be seen increasing with time [Fig. 9(c)]. During $t < 2$ min, the water produced from the reconsolidation could not drain to the surface and resulted in the formation of a water film at the sand–clay interface [Fig. 9(d)]. Consequently, during this period, no surface settlement occurred. The maximum thickness of the water film formed was about 0.5 mm (in model scale). At $t \approx 2$ min, the water film drained once it formed a clear drainage path from the sides of the. As the water film drained, the soil
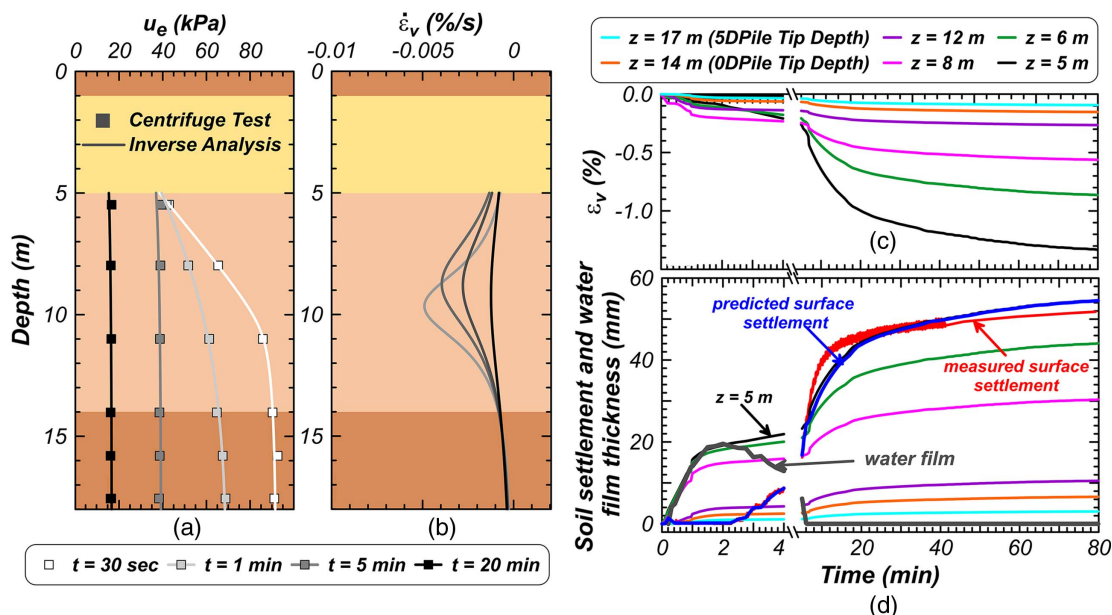
© ASCE   04022111-9   J. Geotech. Geoenviron. Eng.

J. Geotech. Geoenviron. Eng., 2022, 148(12): 04022111

Fig. 9. Inverse analysis of excess pore pressure arrays for shaking event EQM$_3$ of centrifuge test SKS02. Isochrones of (a) excess pore pressure (u_e); and (b) reconsolidation strain rate ($\dot{\varepsilon}v$) at selected times. Time histories of (c) reconsolidation strain (εv); and (d) water film thickness, soil settlement at selected depths and at pile's tip location, and comparison of surface settlement from numerical analysis with centrifuge test results.
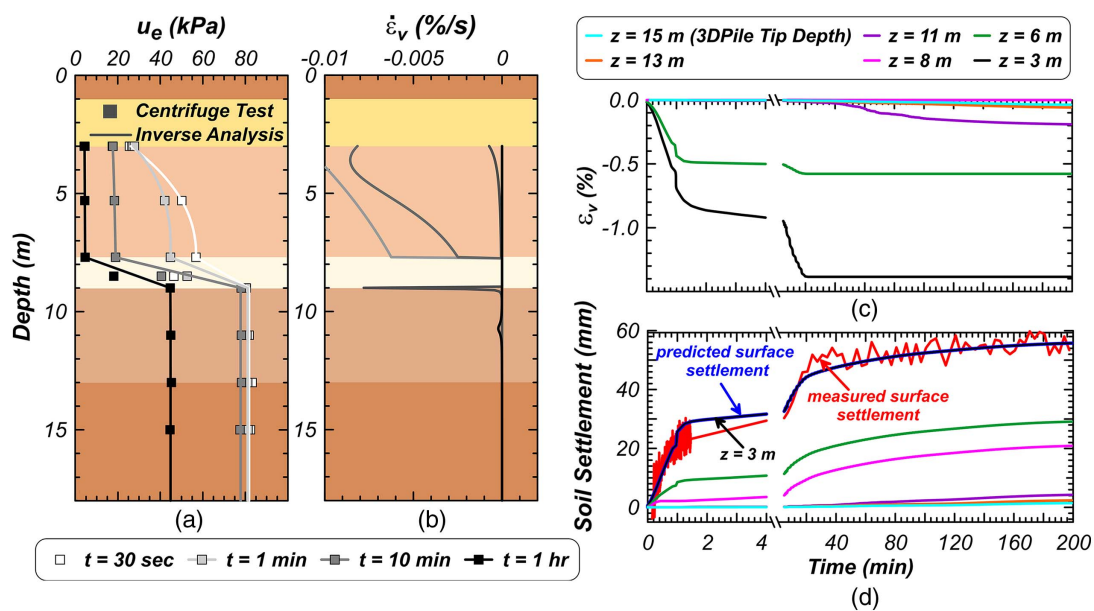

Fig. 10. Inverse analysis of excess pore pressure arrays for shaking event EQM$_4$ of centrifuge test SKS03. Isochrones of (a) excess pore pressure (u_e); and (b) reconsolidation strain rate ($\dot{\varepsilon}v$) at selected times. Time histories of (c) reconsolidation strain (εv); and (d) soil settlement at selected depths and at pile's tip location, and comparison of surface settlement from numerical analysis with centrifuge test results.

surface settled [Fig. 9(d)]. By about 6 min, the water film had entirely dissipated, whereas the reconsolidation continued and lasted for more than an hour. Most of the volume change occurred in the loose sand layer with an average reconsolidation strain of $\varepsilon_v \approx 0.56\%$. The average reconsolidation strain in the dense sand layer was $\varepsilon_v \approx 0.1\%$. The results also show some settlements occurring at the pile's tip depth [Fig. 9(d)]. Soil settlement of about 7 and 3 mm was calculated at the tip of the 0DPile and 5DPile, respectively.

For SKS03, results from the inverse analyses provided insights on the sequencing and timing of soil settlement (Fig. 10). During shaking, the cracks in the weakly cemented crust layer provided quick drainage for the loose sand layer, resulting in soil settlement during and postshaking. As expected from the observation of surface settlement, the numerical analysis results also did not show any water film formation at the sand–clay interface. Complete reconsolidation of the loose sand layer was completed within 20 min [Fig. 10(c)]. Reconsolidation in the medium dense sand layer

© ASCE 04022111-10 J. Geotech. Geoenviron. Eng.

J. Geotech. Geoenviron. Eng., 2022, 148(12): 04022111

started much later (about 20 min) and took more than 2 h to achieve complete reconsolidation. Results from the inverse analysis show that the loose sand and medium dense sand layers developed average reconsolidation strains of 0.75% and 0.48%, respectively. In comparison, the dense sand layer developed an average reconsolidation strain of 0.03%. The results also showed soil settlement of about 1.5 mm at the pile's tip depth [Fig. 10(d)].

Axial Load Distribution and Drag Load

Axial load distributions at selected times obtained from the TzQzLiq analyses were compared against results from the centrifuge tests in Figs. 11–13. Results from the pile embedded three diameters in dense sand with a small pile head load, 3DPileS, are compared in Fig. 11; results from the piles with medium load (3DPileM) and large load (3DPileL) are compared in Fig. 12. Results for the 0DPile and 5DPile are compared in Fig. 13. The free-field effective stress and soil settlement profiles at the selected times are also presented in Figs. 11(a and b) and 13(a and b). Time histories of axial load for the piles at selected depths from the TzQzLiq analysis are compared against results from centrifuge tests in Figs. 11(f), 12(d), and 13(f). The initial axial load

distribution in the TzQzLiq analysis matched the centrifuge test results quite well [$t = 0$ s in Figs. 11(d), 12(a), and 13(a)]. The initial axial load distribution of 3DPileL [Fig. 12(b)] did not match well. An investigation found that some gauges of the 3DPileL (which had already been used as 0DPile in the SKS02 model) might have become unreliable. The gauges of the pile were found to be sensitive to bending moments. They had not performed well in the previous centrifuge test SKS02 (Sinha et al. 2021b). Regardless, it was thought worthwhile to numerically model and study the response of 3DPileL while keeping in mind the lower reliability of the comparisons for 3DPileL.

The axial load in piles decreased during shaking; however, postshaking, it again increased when the excess pore pressures dissipated, and the soil settled. For the SKS03 model, the axial loads in 3DPileS and 3DPileM at different depths and times matched quite well with the measured loads from the centrifuge tests [Figs. 11(d and f) and 12(a and d)]. For 3DPileM, the load near its tip (at a depth of 13.5 m) [Fig. 12(d)] estimated by the numerical model was higher than the measured loads. However, the increments of axial load during reconsolidation ($t > 70$ s) were similar. The difference in the axial load was found to be most apparent during
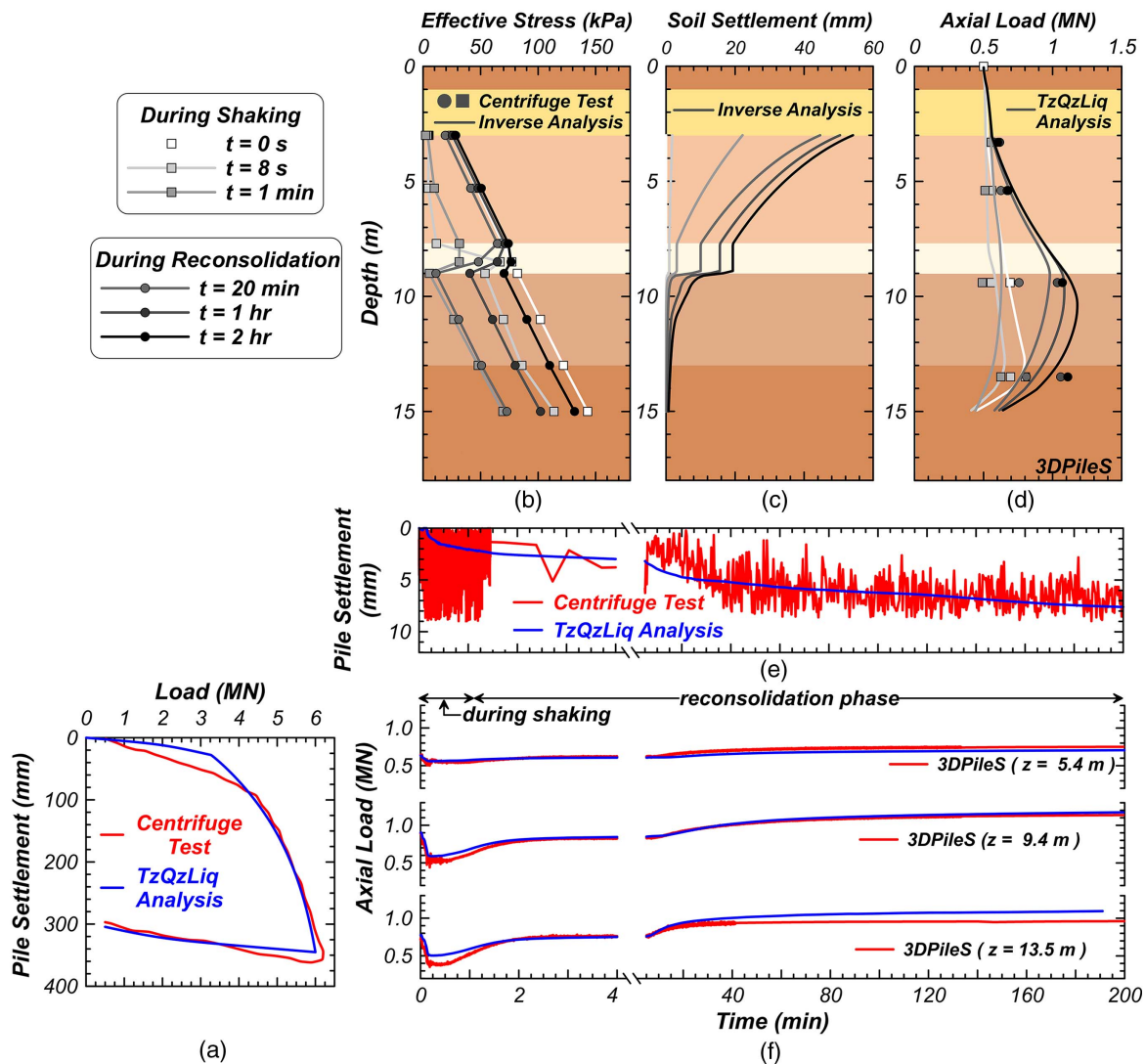

Fig. 11. Validation of TzQzLiq analysis of 3DPileS for shaking event EQM₄ in centrifuge test SKS03: (a) Calibration of QzLiq material properties against pile load test data. Profiles of (b) effective stress; (c) soil settlement; and (d) axial load at selected times during and after shaking. Time histories of (e) settlement; and (f) axial load at the selected depths.
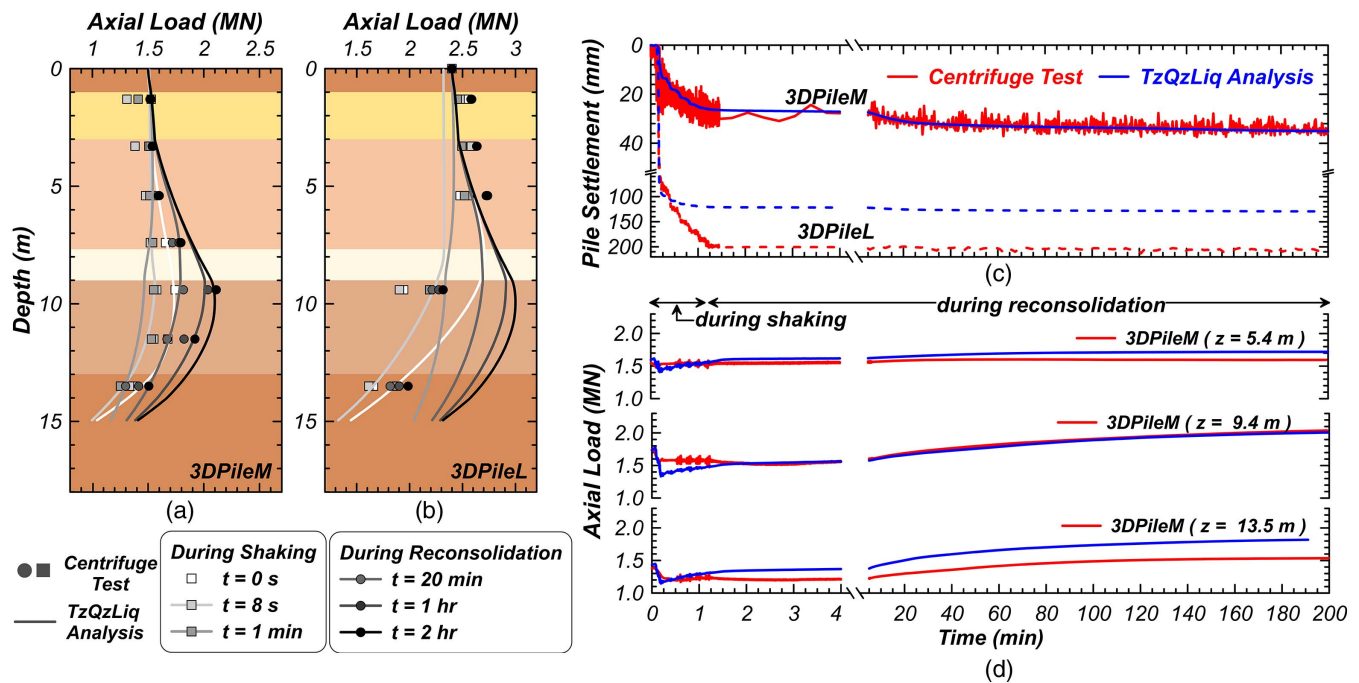
© ASCE   04022111-11   J. Geotech. Geoenviron. Eng.

J. Geotech. Geoenviron. Eng., 2022, 148(12): 04022111

Fig. 12. Validation of TzQzLiq analysis of 3DPileM and 3DPileL for shaking event EQM₄ in centrifuge test SKS03: Axial load profiles of (a) 3DPileM; and (b) 3DPileL at selected times during and after shaking. Time histories of (c) settlement; and (d) axial load of piles at the selected depths.

shaking (i.e., $t < 70$ s). The postshaking axial load distribution in 3DPileL followed a similar load distribution profile as 3DPileM. Similar results were observed from the numerical modeling of SKS02 piles. The disagreement between the axial load increments in the 0DPile and 3DPile is apparent during shaking [Fig. 13(f)]. During reconsolidation, the increments in the axial loads from the numerical analysis were similar to those from the centrifuge test. The deeper gauges of 3DPileL (at the depths of 9.4 and 13.5 m) showed a relatively smaller load than the simulation results. It is still unclear whether the gauges did not work well or some other unexplained mechanism (not modelled in the current simulation) caused the decrease of axial loads. Not modeling the dynamic changes in lateral stresses could be one of the reasons for differences between the numerical and centrifuge test results. Future investigation and developments may be able to explain the observed results. Overall, the axial load distribution in the piles matched reasonably well with the centrifuge test data [Figs. 11(d), 12(a and b), and 13(c and d)].

An increase in excess pore pressure during shaking decreased drag load and correspondingly resulted in a shallow neutral plane (i.e., the depth of maximum axial load). However, as excess pore pressures dissipated and the soil settled, the drag load again increased, and correspondingly the neutral plane deepened. Results from the numerical analysis of time histories of drag load and neutral plane depth for all the piles are shown in Fig. 14. For heavily loaded piles (3DPileM and 3DPileL) and piles with shallow embedment (0DPile), drag load decreased to zero during shaking, and correspondingly the neutral plane reached the ground surface. Changes in the neutral plane for 5DPile and 3DPileS were small. For all the piles, only a few minutes ($<2-3$ min) after shaking, the neutral plane came back close to the initial depth before shaking; however, the increase in drag load was small. During this period, the soil had settled about 10–20 mm. This shows that a small amount of soil settlement during reconsolidation is enough to bring back the neutral plane close to the initial depth before shaking. As

reconsolidation progressed, drag load and depth of the neutral plane both increased. After complete reconsolidation, the drag load was greater for the deeply embedded (5DPile) and the lightly loaded pile (3DPileS). The drag loads on 3DPileM and 3DPileL were equal [Fig. 14(b)], which was also confirmed by the similar axial load distribution during reconsolidation [Figs. 12(a and b)]. The neutral plane depth was greater for piles with deeper embedment. 5DPile developed the deepest neutral plane (14 m). Regardless of different head loads, all the 3DPiles of SKS03 after complete reconsolidation resulted in the same neutral plane depth (~10.5 m). However, the developed drag load on the lightly loaded pile (3DPileS) was 15% (about 100 kN) greater than the other piles (3DPileM and 3DPileL).

Pile Settlement

Settlement time histories of the piles (0DPile, 5DPile, and 3DPiles) from the numerical analysis matched quite well with recorded settlements. The comparisons between the recordings from the centrifuge test and numerically simulated time histories of pile settlement are shown in Figs. 11(e), 12(c), and 13(e). During shaking, although the axial loads in piles at all depths decreased because of the decrease in the initial drag loads from the increased excess pore pressures, the loss of the shaft and tip capacity and its stiffness resulted in the settlement of the piles [Figs. 11(e and f), 12(c and d), and 13(e and f)]. During reconsolidation, as effective stresses increased and the soil settled, the redevelopment of drag load resulted in an additional settlement of the piles. Piles that had a large ratio of static axial capacity to the applied head load (5DPile and 3DPileS) settled <2 mm during shaking and <5 mm during reconsolidation [Figs. 11(e) and 13(e)]. The 0DPile recorded settlement of about 10 mm both during shaking and during reconsolidation. However, during reconsolidation, because the soil at the tip settled by 7 mm [Fig. 9(d)], the penetration of the 0DPile in soil was effectively <5 mm. Heavily loaded piles (3DPileM and 3DPileL) suffered large settlements during shaking (>20 mm). Settlement
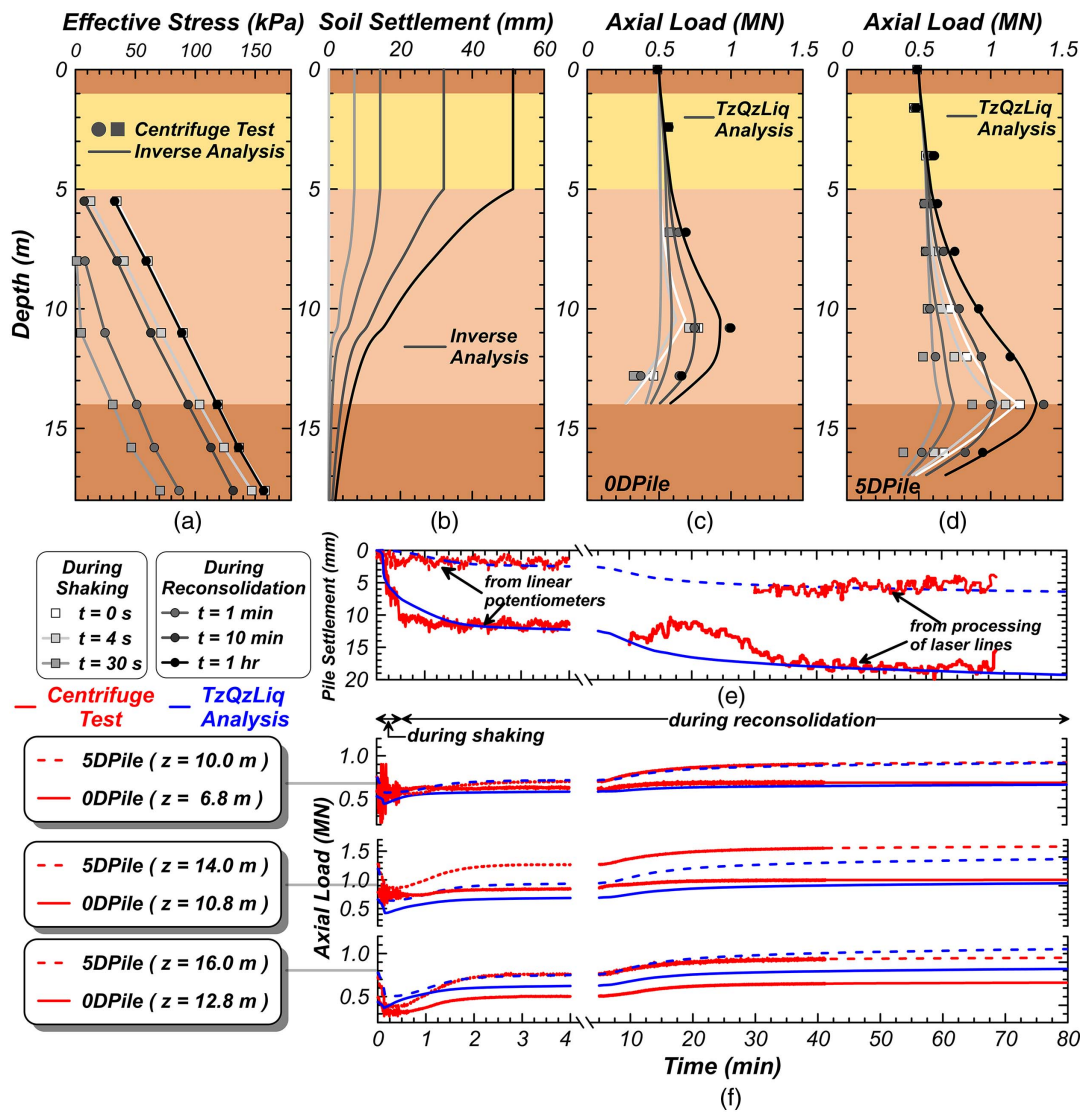
© ASCE   04022111-12   J. Geotech. Geoenviron. Eng.

J. Geotech. Geoenviron. Eng., 2022, 148(12): 04022111

Fig. 13. Validation of TzQzLiq analysis of 0DPile and 5DPile for shaking event EQM$_3$ in centrifuge test SKS02: Profiles of (a) effective stress; (b) soil settlement, and axial load of (c) 0DPile; and (d) 5DPile at selected times during and after shaking. Time histories of (e) settlement; and (f) axial load of piles at the selected depths.
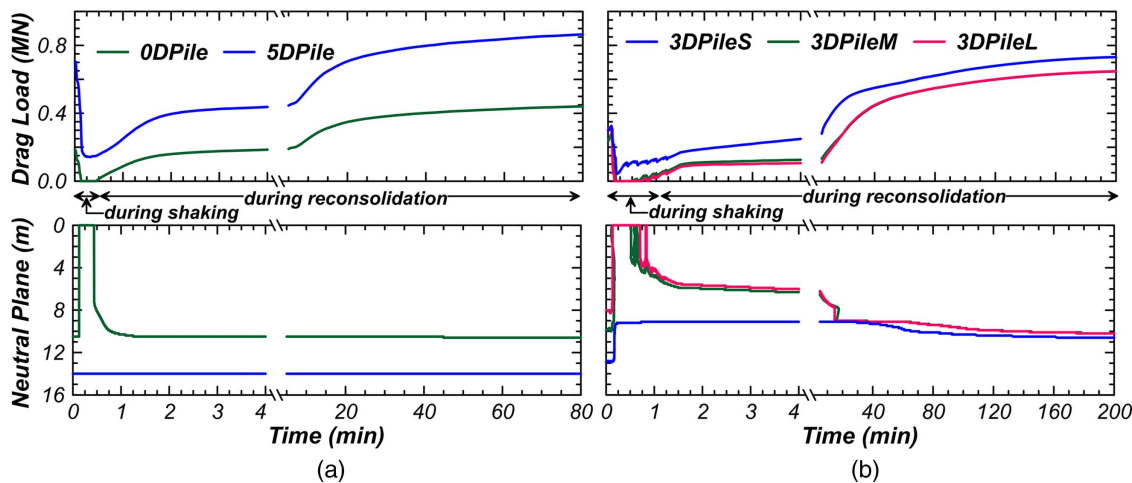

Fig. 14. Results from the TzQzLiq analysis on time histories of drag load and neutral plane (depth of maximum load, Q_{np}) for 0DPile, 5DPile, 3DPileS, 3DPileM, and 3DPileL.

© ASCE 04022111-13 J. Geotech. Geoenviron. Eng.

J. Geotech. Geoenviron. Eng., 2022, 148(12): 04022111

time histories of 3DPileS, 3DPileM, 0DPile, and 5DPile matched the recorded settlement quite well [Figs. 11(e), 12(c), and 13(e)] both during shaking and reconsolidation. For 3DPileL, there were some differences in the numerical and centrifuge test results. Although both the numerical analysis and centrifuge test showed plunging of 3DPileL during shaking, the numerical model under-predicted the settlement of 3DPileL during shaking by about 40% [Fig. 12(c)]. The numerical analysis showed the settlement of the pile to be about 120 mm (i.e., ~19% of the pile's diameter) compared to about 200 mm (~31% of the pile's diameter) in the centrifuge test. A possible explanation for the difference could be the limitation of the constitutive model of the QzLiq material in accurately modeling the realistic behavior of the tip. The exponent (α_t) was assumed constant ($\alpha_t = 0.55$) throughout the analysis; in reality, it may not be a constant; for example, it may increase to 1.0 during failure. Similarly, the parameter (z_{50}) may also not be a constant and increase with the excess pore pressure ratio (r_u). The settlement of 3DPileL during reconsolidation (about 10 mm) matched quite well with the centrifuge test results. The slope of the pile settlement during reconsolidation can be seen parallel to the centrifuge test results [Fig. 12(c)]. Overall, the numerical model with the newly developed QzLiq material reasonably modeled the movement of piles in liquefiable soils both during shaking and reconsolidation. Results showed that the pile settlement mainly

occurred during shaking when the excess pore pressures were high. During reconsolidation, the tip penetration in soil was small (<10 mm). The piles with smaller head loads (3DPileS and 5DPile) suffered settlements less than 10 mm. Other piles settled more than about 20 mm.

Sensitivity Study of TzLiq and QzLiq Material Properties

A sensitivity study on TzLiq and QzLiq material properties was performed to exercise and further increase our understanding of the numerical modeling of liquefaction-induced downdrag on piles. The results from the sensitivity study of the QzLiq exponent (α_t) and TzLiq parameter (z_{50}) on (1) the developed drag load, (2) neutral plane depth, (3) pile settlement, and (4) mobilized tip load (after complete reconsolidation) for the 0DPile, 5DPile, 3DPileS, 3DPileM, and 3DPileS are shown in Figs. 15(a–d), respectively. For each pile, nine simulations were performed, representing the nine data points in each plot in Fig. 15. The x-axis in Fig. 15 represents three scenarios of the TzLiq parameter z_{50} numbered as (1) $z_{50,\text{loose}} = 0.3\%D$ to $z_{50,\text{dense}} = 0.3\%D$, (2) $z_{50,\text{loose}} = 0.3\%D$ to $z_{50,\text{dense}} = 0.15\%D$, and (3) $z_{50,\text{loose}} = 0.6\%D$ to $z_{50,\text{loose}} = 0.15\%D$. Within each of the listed scenarios, three sets of the QzLiq exponent (α_t) were used: $\alpha_t = 0.3$, $\alpha_t = 0.55$, and $\alpha_t = 0.8$.
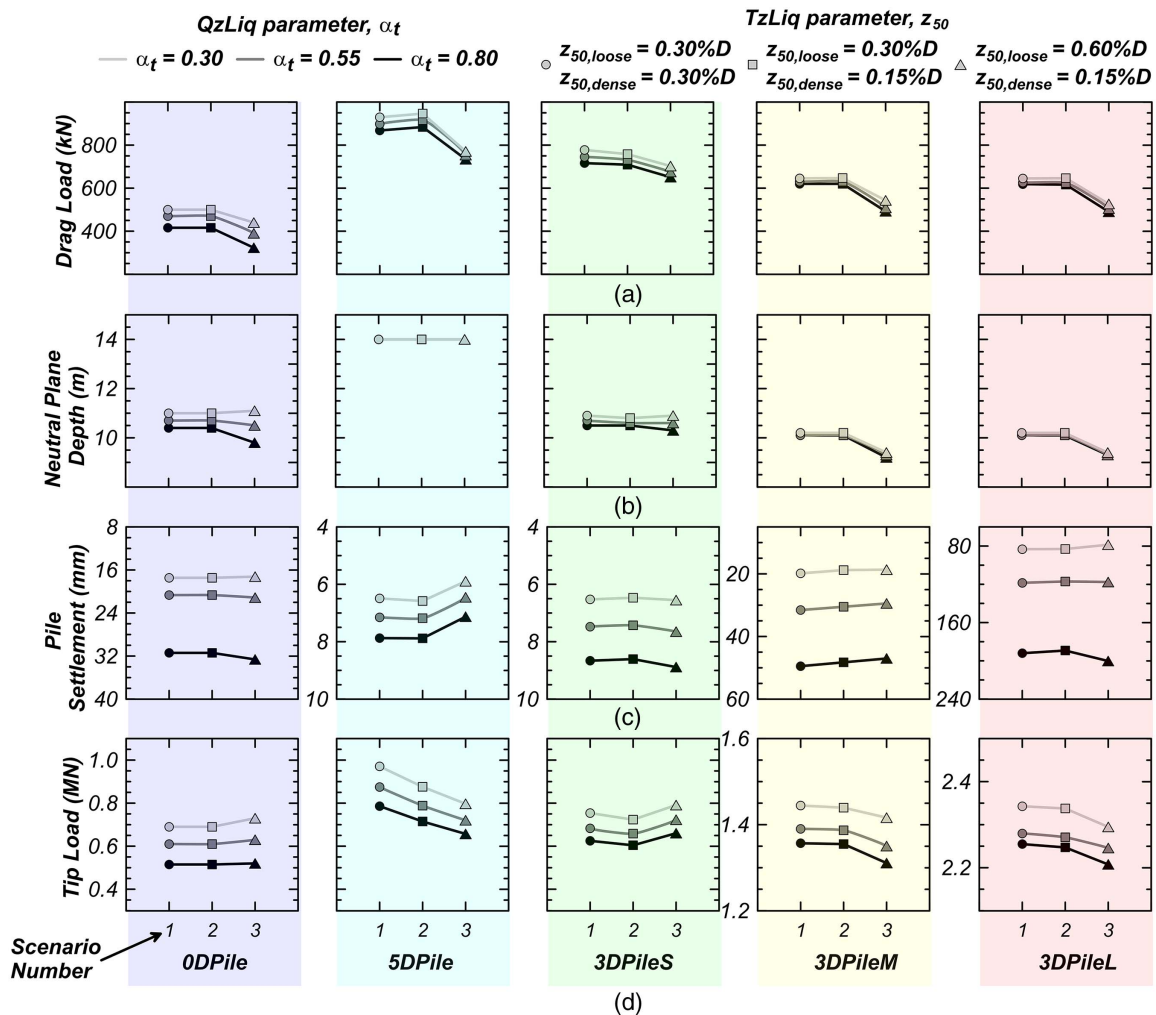

Fig. 15. Results from the sensitivity study of QzLiq constant (α_t) and stiffness of TzLiq material in dense ($z_{50,\text{dense}}$) and loose sand ($z_{50,\text{loose}}$) on (a) drag load; (b) neutral plane depth; (c) pile settlement; and (d) mobilized tip load after complete reconsolidation for 0DPile, 5DPile, 3DPileS, 3DPileM, and 3DPileL for shaking events EQM$_3$ (in centrifuge test SKS02) and EQM$_4$ (in centrifuge test SKS03).

© ASCE 04022111-14 J. Geotech. Geoenviron. Eng.

J. Geotech. Geoenviron. Eng., 2022, 148(12): 04022111

The three different grayscale line plots in Fig. 15 correspond to variations of the QzLiq exponent (α_t).

The sensitivity study showed that the QzLiq material stiffness significantly affects pile settlement. The increase in the QzLiq constant (α_t) (from $\alpha_t = 0.30$ to $\alpha_t = 0.8$) resulted in larger pile settlement [Fig. 15(c)] and decreased drag load [Fig. 15(a)]. Correspondingly, the mobilized tip load [Fig. 15(d)] and the neutral plane depth [Fig. 15(b)] also decreased. Increasing the QzLiq constant (α_t) decreased the tip capacity ($q_{t,\mathrm{ult}}^{r_u}$) and stiffness nonlinearly [Eq. (2)]. A smaller tip capacity and stiffness (i.e., larger α_t) resulted in a larger settlement and a smaller drag load. As expected, the heavily loaded piles (3DPileM and 3DPileL) experienced greater changes in pile settlement than the lightly loaded piles (0DPile, 5DPile, and 3DPileS) as the exponent (α_t) changed [Fig. 15(c)]. The increase in settlement of lightly loaded piles resulted in a decrease in drag load. However, any further increase in pile settlement for heavily loaded piles did not cause any significant change in drag load [Fig. 15(a)].

The sensitivity study showed that the TzLiq material stiffness parameter z_{50} controls the development of drag load. Changes in the stiffness of the TzLiq material in the soil below the neutral plane showed minimal effect on the magnitude of drag load and pile settlement. The decrease in the stiffness of TzLiq material ($z_{50,\mathrm{loose}} = 0.3\%D$ to $z_{50,\mathrm{loose}} = 0.6\%D$) in the loose sand layer significantly decreased drag load [Fig. 15(a)]. Correspondingly, the neutral plane depth [Fig. 15(b)] and mobilized tip load [Fig. 15(d)] also decreased. For the lightly loaded piles (0DPile and 3DPileS) that had their neutral plane in the loose sand layer and thus had a significant contribution to shaft friction in resisting the pile; the decrease of stiffness of TzLiq material resulted in more load transferred to the tip [Fig. 15(d)]. For the heavily loaded piles (3DPileM and 3DPileL) and the piles with a neutral plane below the loose sand layer (5DPile), the decrease in stiffness of TzLiq material decreased the overall load at the neutral plane, causing smaller mobilization of load at the tip [Fig. 15(d)]. The increase in the stiffness of TzLiq material in dense sand layer ($z_{50,\mathrm{dense}} = 0.30\%D$ to $z_{50,\mathrm{dense}} = 0.15\%D$) showed minimal effect on the drag load [Fig. 15(a)] and pile settlement [Fig. 15(c)]. The dense sand layer being below the neutral plane did not contribute to drag load. For the 5DPile, a higher stiffness of TzLiq material mobilized greater shaft friction in the dense sand and resulted in a smaller load transferred to the tip [Fig. 15(d)]. For the piles not embedded very deep in dense sand, the increased TzLiq stiffness in dense sand had minimal effect.

Considerations for Practice

The paper used the centrifuge test data to determine the effective stress and soil settlement profiles and TzLiq and QzLiq material properties. In practice, one would need to determine the pore pressure and free-field settlement distribution by other analysis procedures. For example, a 1D site response analysis with pore pressure models [such as Chiaradonna et al. (2020)] with the design earthquake followed by a reconsolidation analysis could be a reasonable approach for predicting the effective stress and soil settlement distributions over the depth. The ultimate capacity of TzLiq and QzLiq materials can be obtained from the empirical correlations developed on data from soil investigation methods such as cone penetration tests, static penetration tests, and others. The stiffness of TzLiq material can be defined considering that a small relative displacement of 10–30 mm or 1%–3% of the pile's diameters is enough to mobilize the full shaft resistance in piles (Sinha et al. 2022b). Determining site-specific QzLiq material stiffness is essential for

accurately modeling pile settlement and drag load. The sensitivity study shows that the stiffness of the QzLiq material significantly affects the pile settlement. On the other hand, the drag load is affected by the stiffness of both the TzLiq and the QzLiq material. Therefore, it is crucial to calibrate the initial capacity and stiffness properties of the QzLiq material against results from the pile load test. In the absence of test data, displacement equal to 10% of pile diameter can be taken as the tip penetration required to mobilize the capacity of QzLiq material (API 2000). The constant (α_t) for the QzLiq material can be estimated from Eq. (2). Additionally, a sensitivity study can be performed on the stiffness of the TzLiq and QzLiq material to determine their effect on pile settlement and drag load.

The TzQzLiq numerical model presented in the paper can model the response of piles during shaking and reconsolidation. Analysis results on the axial load distribution, pile settlement, and drag load can aid in designing and evaluating the performance of piles in liquefiable soils. The maximum load obtained on the pile (Q_{np}) at the end of reconsolidation can be checked against the pile's structural strength. In addition, the settlement of the pile at the end of shaking and after complete reconsolidation can be checked against the serviceability criteria. Sinha et al. (2022c) and Sinha (2022) used the results from the centrifuge tests and the proposed TzQzLiq numerical modeling procedure (presented in this paper) as a basis to develop a simplified procedure for designing piles in liquefiable soils.

Summary and Conclusions

A TzQzLiq numerical analysis was performed to model liquefaction-induced downdrag on piles. Model input parameters included TzLiq and QzLiq material properties, time histories of soil settlement and effective stress profiles, and pile properties. A QzLiq material was developed and implemented in OpenSees to model the reduction of pile tip capacity and stiffness in the presence of excess pore pressures. Together, the TzLiq and the QzLiq materials account for changes in the shaft and the tip capacity of the pile as free-field excess pore pressures develop and dissipate in soil. The TzLiq and the QzLiq material properties were obtained and calibrated against the limit load curves and pile load test results. The TzQzLiq analysis was validated against the results from a series of large centrifuge model tests conducted on piles embedded in layered and interbedded soil deposits with liquefiable layers. An inverse analysis was performed on the measured excess pore pressure arrays to obtain time histories of soil settlement profiles. The results showed that the TzQzLiq analysis reasonably predicted the time histories of axial load distribution and settlement of piles.

A numerical model was developed and incorporated into the inverse analysis of the centrifuge model test to study the water film formation at the sand–clay interface. The formation and drainage of the water film were modeled as the net velocity of water ($q_{\mathrm{in}} - q_{\mathrm{out}}$) entering or leaving the interface. The results from the numerical model explained the mechanism behind the observed surface settlement in the centrifuge test SKS02. Although the impermeable clay layer hindered drainage, the dissipation of excess pore pressures (and reconsolidation) occurred in the loose sand layer resulting in the formation of the water film. During this period, no surface settlement occurred in the model. However, once the water established drainage paths through cracks or along the edges of the model container, the water film started draining, and the surface settled. Time histories of the numerically simulated surface settlement matched well the recorded measurements from the centrifuge test.

© ASCE 04022111-15 J. Geotech. Geoenviron. Eng.

J. Geotech. Geoenviron. Eng., 2022, 148(12): 04022111

The TzQzLiq analysis improves the traditional neutral plane solution method by accounting for changes in the stiffness and capacity of the pile's shaft friction and tip resistance in liquefiable soils, offering complete modeling of the liquefaction-induced downdrag phenomenon, and provides a time history of axial load distribution and settlement of piles. Further improvements to the analysis may include accounting for dynamic changes of lateral stresses during and after shaking and more realistic modeling of QzLiq material constant (α_t). The effective lateral stresses may not be constant and may depend on the mobilized radial stresses and dilatancy around the pile's interface. Moreover, changes in lateral stresses during shaking might differ from during reconsolidation. The QzLiq material constant α_t and z_{50} may also change with dilation near the tip. As research continues, filling these modeling gaps will further improve the numerical model in better capturing the axial load distribution and settlement of piles.

Data Availability Statement

Some or all data, models, or code generated or used during the study are available in a repository online following the funding agency's data retention policies. The centrifuge test data used in this study are made available through DesignSafe under Project PRJ-2828. https://www.designsafe-ci.org/data/browser/public/designsafe.storage.published/PRJ-2828.

Acknowledgments

References

AASHTO. 2020. *AASHTO LRFD bridge design specifications*. LRFDUS-9. Washington, DC: AASHTO.

API (American Petroleum Institute). 2000. *Recommended practice for planning, designing and constructing fixed offshore platforms—Working stress design*. API Recommended Practice 24-WSD. Washington, DC: API.

Boulanger, R. W., and S. J. Brandenberg. 2004. "Neutral plane solution for liquefaction-induced down-drag on vertical piles." In *GeoTrans*, Geotechnical Special Publication 126, edited by M. K. Yegian and E. Kavazanjian, 470–478. Reston, VA: ASCE. https://doi.org/10.1061/40744(154)32.

Boulanger, R. W., C. J. Curras, B. L. Kutter, D. W. Wilson, and A. Abghari. 1999. "Seismic soil-pile-structure interaction experiments and analyses." *J. Geotech. Geoenviron. Eng.* 125 (9): 750–759. https://doi.org/10.1061/(ASCE)1090-0241(1999)125:9(750).

Caltrans. 2020. "Liquefaction-induced downdrag." *Caltrans Geotechnical Manual*. Accessed February 07, 2020. https://dot.ca.gov/programs/engineering-services/manuals/geotechnical-manual.

Chiaradonna, A., A. Flora, A. d'Onofrio, and E. Bilotta. 2020. "A pore water pressure model calibration based on in-situ test results." *Soils Found.* 60 (2): 327–341. https://doi.org/10.1016/j.sandf.2019.12.010.

De Beer, E. 1967. "Proefondervindelijke Bijdrage tot de Studie van zand onder funderingern op stall." In *Tijdshrift der Openbar Werken van het grensdraag vermogen van Beigie, Nos. 6–1967, and 6–1968*. Ghent, Belgium: NICI.

Elvis, I. 2018. "Liquefaction-induced dragload and/or downdrag on deep foundations within the New Madrid seismic zone." Ph.D. dissertation, Dept. of Civil Engineering, Univ. of Arkansas.

Fellenius, B. H. 1972. "Down-drag on piles in clay due to negative skin friction." *Can. Geotech. J.* 9 (4): 323–337. https://doi.org/10.1139/t72-037.

Fellenius, B. H. 2004. "Unified design of piled foundations with emphasis on settlement analysis." In *GeoTrans 2004: Current Practices and Future Trends in Deep Foundations*, Geotechnical Special Publication 125, edited by J. A. DiMaggio and M. H. Hussein, 253–275. Reston, VA: ASCE. https://doi.org/10.1061/40743(142)15.

Fellenius, B. H., B. Abbasi, and B. Muhunthan. 2020. "Liquefaction induced downdrag for the Juan Pablo II bridge at the 2010 Maule earthquake in Chile." *Geotech. Eng. J. SEAGS AGSSEA* 51 (2): 1–8.

Fellenius, B. H., and T. C. Siegel. 2008. "Pile drag load and downdrag in a liquefaction event." *J. Geotech. Geoenviron. Eng.* 134 (9): 1412–1416. https://doi.org/10.1061/(ASCE)1090-0241(2008)134:9(1412).

Fiegel, G. L., and B. L. Kutter. 1994. "Liquefaction mechanism for layered soils." *J. Geotech. Eng.* 120 (4): 737–755. https://doi.org/10.1061/(ASCE)0733-9410(1994)120:4(737).

Fleming, K., A. Weltman, M. Randolph, and K. Elson. 2008. *Piling engineering*. London: CRC Press. https://doi.org/10.1201/b22272.

Gajan, S., P. Raychowdhury, T. C. Hutchinson, B. L. Kutter, and J. P. Stewart. 2010. "Application and validation of practical tools for nonlinear soil-foundation interaction analysis." *Earthquake Spectra* 26 (1): 111–129. https://doi.org/10.1193/1.3263242.

Garnier, J., C. Gaudin, S. M. Springman, P. J. Culligan, D. Goodings, D. Konig, B. Kutter, R. Phillips, M. F. Randolph, and L. Thorel. 2007. "Catalogue of scaling laws and similitude questions in geotechnical centrifuge modelling." *Int. J. Phys. Model. Geotech.* 7 (3): 1–23. https://doi.org/10.1680/ijpmg.2007.070301.

Hannigan, P. J., F. Rausche, G. E. Likins, B. R. Robinson, and M. L. Becker. 2016. *Design and construction of driven pile foundations*. Rep. No. FHWA-NHI-16-009. Woodbury, MN: Federal Highway Administration.

Khosravifar, A., and R. W. Boulanger. 2010. "Inelastic response of extended pile shafts in laterally spreading ground during earthquakes (student paper competition 2010)." *DFI J.* 4 (2): 41–53. https://doi.org/10.1179/dfi.2010.009.

Knappett, J. A., and S. P. G. Madabhushi. 2009. "Seismic bearing capacity of piles in liquefiable soils." *Soils Found.* 49 (4): 525–535. https://doi.org/10.3208/sandf.49.525.

Kokusho, T. 1999. "Water film in liquefied sand and its effect on lateral spread." *J. Geotech. Geoenviron. Eng.* 125 (10): 817–826. https://doi.org/10.1061/(ASCE)1090-0241(1999)125:10(817).

Kokusho, T. 2000. "Mechanism for water film generation and lateral flow in liquefied sand layer." *Soils Found.* 40 (5): 99–111. https://doi.org/10.3208/sandf.40.5_99.

Lehane, B. M., J. A. A. Schneider, and X. Xu. 2005. *A review of design methods for offshore driven piles in siliceous sand*. GEO:05358 ed. Perth, Australia: Univ. of Western Australia.

Malvick, E. J., R. Kulasingam, R. W. Boulanger, and B. L. Kutter. 2002. *Effects of void redistribution on liquefaction flow of layered soil—Centrifuge data report for EJM01*. Rep. No. UCD/CGMDR-02/02. Davis, CA: Center for Geotechnical Modeling, Univ. of California Davis.

Malvick, E. J., B. L. Kutter, and R. W. Boulanger. 2008. "Postshaking shear strain localization in a centrifuge model of a saturated sand slope." *J. Geotech. Geoenviron. Eng.* 134 (2): 164–174. https://doi.org/10.1061/(ASCE)1090-0241(2008)134:2(164).

McKenna, F., M. H. Scott, and G. L. Fenves. 2010. "Nonlinear finite-element analysis software architecture using object composition." *J. Comput. Civ. Eng.* 24 (1): 95–107. https://doi.org/10.1061/(ASCE)CP.1943-5487.0000002.

Mosher, R. L. 1984. *Load-transfer criteria for numerical analysis of axially loaded piles in sand*. Rep. No. K-84. Vicksburg, MS: US Army Engineer Waterways Experiment Station.

Muhunthan, B., N. V. Vijayathasan, and B. Abbasi. 2017. *Liquefaction-induced downdrag on drilled shafts*. Rep. No. WA-RD 865.1. Pullman, WA: Washington State DOT.

© ASCE 04022111-16 J. Geotech. Geoenviron. Eng.

J. Geotech. Geoenviron. Eng., 2022, 148(12): 04022111

Nicks, J. 2017. *Liquefaction-induced downdrag on continuous flight auger (CFA) piles from full-scale tests using blast liquefaction*. Rep. No. FHWA-HRT-17-060. McLean, VA: Federal Highway Administration.

OpenSees Documentaion. 2021. "QzLiq1 Material." Accessed December 9, 2021. https://opensees.github.io/OpenSeesDocumentation/user/manual/material/uniaxialMaterials/QzLiq1.html.

Reese, L. C., and M. W. O'Niel. 1987. *Drilled shafts: Construction procedures and design methods*. Rep. No. FHWA-IF-99-025. Mclean, Virginia: Federal Highway Administration.

Rollins, K. 2017. "Dragload and downdrag on piles from liquefaction induced ground settlement." In *Proc., US–New Zealand–Japan Int. Workshop on Liquefaction-Induced Ground Movement Effects*, edited by J. D. Bray, R. W. Boulanger, M. Cubrinovski, K. Tokimatsu, S. L. Kramer, T. O'Rourke, R. A. Green, P. K. Robertson, and C. Z. Beyzaei. Berkeley, CA: Pacific Earthquake Engineering Research Center, Univ. of California Berkeley.

Rollins, K. M., and J. E. Hollenbaugh. 2015. "Liquefaction induced negative skin friction from blast-induced liquefaction tests with auger-cast piles." In *Proc., 6th Int. on Conf. Earthquake Geotechnical Engineering*. London: International Society for Soil Mechanics and Geotechnical Engineering.

Rollins, K. M., and S. R. Strand. 2006. "Downdrag forces due to liquefaction surrounding a pile." In *Proc., 8th National Conf. on Earthquake Engineering*. Oakland, CA: Earthquake Engineering Research Institute.

Salgado, R., and J. Lee. 1998. *Pile design based on cone penetration tests*. Rep. No. FHWA/IN/JTRP-99/8. West Lafayette, IN: Joint Transportation Research Program, Indiana DOT.

Sinha, S. K. 2022. "Liquefaction-induced downdrag on piles: Centrifuge and numerical modeling, and design procedures." Ph.D. dissertation, Dept. of Civil and Environmental Engineering, Univ. of California Davis.

Sinha, S. K., K. Ziotopoulou, and B. L. Kutter. 2019. "Parametric study of liquefaction induced downdrag on axially loaded piles." In *Proc., 7th Int. Conf. on Earthquake Geotechnical Engineering*. London: International Society for Soil Mechanics and Geotechnical Engineering.

Sinha, S. K., K. Ziotopoulou, and B. L. Kutter. 2021a. *Centrifuge testing of liquefaction-induced downdrag on axially loaded piles: Data report for SKS02*. Rep. No. UCD/CGMDR–21/01. Davis, CA: Center for Geotechnical Modeling, Univ. of California Davis.

Sinha, S. K., K. Ziotopoulou, and B. L. Kutter. 2021b. *Centrifuge testing of liquefaction-induced downdrag on axially loaded piles: Data report for SKS03*. Rep. No. UCD/CGMDR–21/02. Davis, CA: Center for Geotechnical Modeling, Univ. of California Davis.

Sinha, S. K., K. Ziotopoulou, and B. L. Kutter. 2022a. "Centrifuge model tests of liquefaction-induced downdrag on piles." In *Proc., 20th Int. Conf. on Soil Mechanics and Geotechnical Engineering*. London: International Society for Soil Mechanics and Geotechnical Engineering.

Sinha, S. K., K. Ziotopoulou, and B. L. Kutter. 2022b. "Centrifuge model tests of liquefaction-induced downdrag on piles in uniform liquefiable deposits." *J. Geotech. Geoenviron. Eng.* 139 (9): 04022048. https://doi.org/10.1061/(ASCE)GT.1943-5606.0002817.

Sinha, S. K., K. Ziotopoulou, and B. L. Kutter. 2022c. "Displacement-based design of axially loaded piles for seismic loading and liquefaction-induced downdrag." *J. Geotech. Geoenviron. Eng.*

Strand, S. 2008. "Liquefaction mitigation using vertical composite drains and liquefaction-induced downdrag on piles: Implication for deep foundation design." Ph.D. dissertation, Dept. of Civil and Environmental Engineering, Brigham Young Univ.

Titi, H., and M. Y. Abu-Farsakh. 1999. *Evaluation of bearing capacity of piles from cone penetration test data*. LTRC Project No. 98-3GT. Baton Rouge, LA: Dept. of Transportation and Development.

Vijayaruban, V. N., B. Muhunthan, and B. H. Fellenius. 2015. "Liquefaction-induced downdrag on piles and drilled shafts." In *Proc., 6th Int. Conf. on Earthquake Geotechnical Engineering*. London: International Society for Soil Mechanics and Geotechnical Engineering.

Vijivergiya, V. N. 1977. "Load-movement characteristics of piles." In Vol. 2 of *Proc., 4th Symp. of Waterway, Port, Coastal and Ocean Division*, 269–284. New York: ASCE.

Wang, R., and S. J. Brandenberg. 2013. "Beam on nonlinear Winkler foundation and modified neutral plane solution for calculating downdrag settlement." *J. Geotech. Geoenviron. Eng.* 139 (9): 1433–1442. https://doi.org/10.1061/(ASCE)GT.1943-5606.0000888.

Wang, R., W. Cao, S. Brandenberg, and J.-M. Zhang. 2015. "Calculation method of axial force and settlement of pile foundation during foundation consolidation and reconsolidation." *Chin. J. Geotech. Eng.* 37 (3): 512–518. https://doi.org/10.11779/CJGE201503015.

Ziotopoulou, K., S. K. Sinha, and B. L. Kutter. 2022. "Liquefaction-induced downdrag on piles: Insights from a centrifuge and numerical modeling program." In *Proc., 4th Int. Conf. on Performance Based Design in Earthquake Geotechnical Engineering*. London: International Society for Soil Mechanics and Geotechnical Engineering.

© ASCE 04022111-17 J. Geotech. Geoenviron. Eng.

J. Geotech. Geoenviron. Eng., 2022, 148(12): 04022111